FAST HIGH QUALITY SPECKLE-FREE PHASE COMPUTER GENERATED HOLOGRAPHIC IMAGE PROJECTION

by

Deniz Mengü

A Thesis Submitted to
the Graduate School of Engineering and Science
in Partial Fulfillment of the Requirements for
the Degree of

Master of Science

in

Electrical and Electronics Engineering

Koç University

July 2016

Koç University
Graduate School of Science and Engineering

This is to certify that I have examined this copy of a masters thesis by

Deniz Mengü

and have found that it is complete and satisfactory in all respects,
and that any and all revisions required by the final
examining committee have been made.

Committee Members:

____
Prof. Dr. Hakan Ürey(Advisor)

____
Assist. Prof. Dr. Fehmi Çivitçi

____
Assist. Prof. Dr. Fatih Toy

Date: ____________________

ABSTRACT

FAST HIGH QUALITY SPECKLE-FREE PHASE COMPUTER GENERATED HOLOGRAPHIC IMAGE PROJECTION

Deniz Mengü
M.S. in Electrical and Electronics Engineering
Advisor: Prof. Dr. Hakan Ürey
July 2016

Computer generated holography based image projection, 3D television, head-up and near-to-eye (N2E) display systems offer unique advantages over conventional schemes and constitute a promising option for the future of display technology. Such systems provide much higher light efficiency, eliminate the need for bulky optics and provide natural 3D experience.

Computer generated holograms (CGHs) are displayed on spatial light modulators (SLMs) illuminated by coherent light. Ideally, each pixel of an SLM should provide simultaneous and independent amplitude and phase modulation since CGHs are in general complex-valued functions. However, current state of the art SLM technology allows the implementation of only a constrained set of complex values depending on the device type, such as binary amplitude, binary phase, amplitude-mostly or phase-only. Among various types, liquid crystal-on-silicon (LCoS) phase-only SLMs provide the most convenient option due to their smaller pixel pitch, higher diffraction efficiency and 8-bit modulation depth. Yet, these devices become useful only when they are combined with algorithms that encode a full-complex SLM pattern into a phase-only SLM pattern.

In the context of holographic image projection, existing algorithms for phase CGH computation are iterative optimization procedures that require successive transformations with high computational costs. As higher pixel counts are attained, the computational load of iterative methods become increasingly excessive, hindering real-time video applications. Despite their high cost though, the reconstruction performance of these algorithms are only moderate, with generated images suffering significantly from

speckle noise.

In this thesis, two novel phase CGH computation algorithms are proposed. The first algorithm removes the iteration requirement and provides a direct solution, significantly improving the computational efficiency. The second algorithm processes a given desired image and non-iteratively calculates a phase CGH which, when used as a starting point, lets iterative algorithms to converge to almost global optimum, significantly improving reconstruction quality.

The first algorithm is based on the observation that two phase-only pixels are equivalent to a full complex pixel; thus, the SLM is expected to reconstruct half of the desired image samples exactly. Simple Discrete Fourier Transform (DFT) and multirate signal processing relations are utilized to non-iteratively determine a phase CGH that exactly reconstructs the even (or odd) rows (or columns) of a given image. By requiring only a single Fast Fourier Transform (FFT) and a few additional trivial matrix operations, the algorithm offers 6 to 20 times improvement on computational efficiency compared to conventional procedures. The simulation results and proof-of-concept experiments indicate that our algorithm can provide full field-of-view (FOV), low speckle image reconstructions with maximized light efficiency when the reconstructions of 4 CGHs are averaged. High quality frames in the interlaced video format is already deliverable with 60Hz SLMs when the FOV in one direction is reduced to half.

In the second algorithm, we developed a procedure for designing an image specific phase function that leads to an ideal CGH that is almost readily unit magnitude, resulting in a very low quantization error to begin with. When the phase CGH obtained in the described way is used as the starting point for existing iterative algorithms, much quicker convergence and unprecedentedly low reconstruction errors are achieved. The simulations and experiments reveal that reconstruction quality improves by about 20 times compared to iterative algorithms starting from random guesses. The reconstructions are almost speckle free, while allowing maximum light efficiency and FOV.

The developed methods are particularly novel over existing approaches in that full physical as well as mathematical insight is exploited in their development. In particular, while most approaches formulate the phase CGH computation problem as a purely mathematical optimization problem, our methods recognize and utilize the correspondence between phase functions, ray directions, lenses, prisms and so forth. As a result, we can non-iteratively determine phase CGHs that are almost ready, i.e., can perform the desired reconstructions already with low error. In this way, we significantly reduce the number of iterations required, i.e., our methods require iterations just for fine-tuning, whereas in existing algorithms iterations are required for both coarse and fine tuning. Meanwhile, we can get much closer to global optimums than any other method. In this respect, we believe that this thesis also contributes significantly to the understanding of the fundamental limits of phase-only computer holography.

Keywords: Computer Generated Hologram, Spatial Light Modulators, Holographic Displays, Fourier Optics, Phase-Space Distributions, Phase-only Encoding Algorithms.

ÖZET

TÜRKÇE BAŞLIK

Deniz Mengü
Elektrik ve Elektronik Mühendisliği, Yüksek Lisans
Tez Danışmanı: Prof. Dr. Hakan Ürey
Temmuz 2016

Bilgisayarda yaratılan hologramlara dayalı görüntü projeksiyonu teknolojisi, 3D televizyon, ba üstü göstergeleri ve kafaya takılan ekran (N2E) sistemlerinde kullanıldığında sunduğu kendine özgü avantajlarıyla geleceğin ekran uygulamalarında önemli bir rol alması olasılığı yükselmekte olan bir tekniktir. Enerji verimliliği, ağır ve hantal optik elemanlarına ihtiyacı ortadan kaldırabilmesi ve doğal üç boyutlu görüntü sağlayabilmesi bu avantajlardan öne çıkanlardır.

Bilgisayarda yaratılan hologramlar (CGHs) uzamsal ışık modülatörleri (SLM) üzerinde gösterilirler, bu cihazlar da evreuyumlu ışıkla aydınlatılırlar. İdealinde, SLMlerin tüm pikselleri bağımsız ve eş zamanlı bir biçimde ışığın hem fazı hem de büyüklüğünü modüle edebilmelidirler. Ancak, şu an kullanılan SLM teknolojisi yalnızca bazı kısıtlı modülasyon tekniklerine izin vermektedir. Piyasada ikili büyüklük, ikili faz veya sadece faz modülasyonu yapabilen cihazlar bulunmaktadır. Bu çeşitlerin arasından, kücük piksel genişliği, kırınım verimliliği ve 256 farklı seviyede modülasyon derinliği sunmalarıyla yalnız faz modülasyonu yapabilen SLMler dikkat çeker. Bununla birlikte, bu aletlerin laboratuvarlardan çıkarak hayatımıza faydalı olabilmeleri için, tam karmaşık hologramları yalnız faz yapılarna dönüştürecek algoritmalara ihtiyaç duyulmaktadır.

Holografik görüntü projeksiyonu konusunda varolan algoritmalar tekrarlı optimizasyon prosedürleri olarak karşımıza çıkmakta ve arka arkaya yapılan dönüşümlerle hesaplama yükünü fazlasıyla artırmaktadır. Modern SLMlerin piksel sayıları arttıkça, bu yük daha da artmış ve gerçek zamanlı video projeksiyonu için kullanımı olumsuz etkilemiştir. Dahası, görüntü kalitesi olarak da orta seviyenin ilerisine gidememiş, görüntülerde beneklenmeye sebep olmaktadırlar.

Bu tezde, iki yeni faz CGH hesaplama algoritması önerilmiştir. İlki tekrarlı Fourier dönüşümlerine gereksinimi ortadan kaldırmış ve hesaplama verimliliğini

önemli ölcüde geliştirmiştir. İkinci algoritmada ise, istenen görüntüye özel bir faz tasarımı ile SLM üzerinde enerji dağılımı kontrol edilerek optimum çözüme daha önce literatürde rastlanmamış kadar yaklaşılmıştır.

İlk metodumuz, bir ya da iki Hızlı Fourier Dönüşümü (FFT) ile yüksek kalitede görüntüler yaratmayı başarırken, bunu önceki yöntemlere kıyasla 6 ila 20 kat daha hızlı gerçekleştirmektedir.

Tezde sunulan ikinci metod ise, yaratılmak istenen görüntüye özel bir faz fonksiyonu tasarımı önermektedir. Yapılan deney ve simülasyonlar 20 kata kadar kalite gelişimi sağladığını ortaya koymuştur.

Anahtar sözcükler: .

Acknowledgment

I would like to thank my advisor Prof. Hakan Ürey who believed in me, supported, encouraged and provided guidance in every step of this thesis. Although I did not get chance to work closely, I would also like to thank Assoc. Prof. Göksenin Yaralıoğlu for sharing some of the work load in OML with Prof. Ürey. I would also like to thank Asst. Prof. Fatih Toy and Asst. Prof. Fehmi Çivitçi for reading and commenting on this thesis. Besides, during the days Dr. Çivitçi spent in OML, I was inspired by his curiosity and passion for science,so I would like thank him for that as well.

I owe every happiness, joy and success in my life to my dear parents, Özden Mengü and Derya Mengü. Needles to say, they have supported and encouraged me throughout my life and this thesis is dedicated to them as an appreciation for always being there for me. I love you guys. I also thank my **cousin** İrem for joyful conversations and I apologize for not calling her more frequently but if I did I might not be writing that acknowledgement at the moment.

I did not think of myself as a lucky person, but having the opportunity to meet, get to know and work with Dr. Erdem Ulusoy has proven that wrong. I am very lucky indeed. He has not only been my mentor and supervisor during this thesis but I also feel that he is closer than a big brother to me. Obviously, I have learnt so much from him on optics, signal processing and math but he has also taught me a lot on the other aspects of life and science. I hope I will be even luckier to get my second chance to see and talk to him on daily basis again at some point in my life.

There are many people to mention in OML who somehow, not knowingly contributed to that thesis. To begin with, I would like to thank Dr. Kaan Akşit and Osman Eldeş for his help during my orientation to the lab. I am thankful to meet Amir Ghanbariniaki, Sven Holmstrom, Mahdi Kazempour Radi and Selim Öleçer (Selim Abi), their work discipline and enthusiasm is really inspiring. I also thank Yusuf Samet Yaraş and Mehmet Serhan Can for being the Sabanci crew and asking many questions about myself and life, it really pushed me into a rethinking process. I would like to thank Bacsar Batu Can for all his support during the time I was trying to reconstruct his initial letter 'B' holographically and his friendship. Dr. Onur Çakmak and soon to be a PhD. Ulaş Adiyan, I would like to thank you guys for your humorous jokes and skits, you have been making, Ulaş still does, workdays much more fun. I would like to thank Emre Heves for sharing joyful notes, videos and news with me. I am also thankful for the chance to work with Hazal Er. I missed her since she is gone because beside being an excellent team player, she is very kind and amusing. Even though we could not spent much time together, I would like to thank Ali Bars Gündüz and Deniz Ekin Canbay for the discussions outside the lab, Shoaib Soomro for the delicious Pakistani food he cooked for us. One other inspiring personality in the lab is Uğur Aygün. As he does not lose his focus and let the obstacles to affect his happiness, I really enjoyed his friendship, I hope to we can get together soon. I know he would not care that I mention his name or not, but I am sincerely happy to know Mehmet Kıvanç Hedili. His out-of-the-box thinking, sincere personality and fruitful character is really admirable to me. Although she is not an OML member, I would like to thank Gizem Güzelsoy for the joyful discussions right outside of our lab, her easy-going and talkative character and all the great plays that we have been to during the last few years.

Finally, I would like to thank my 'brother', Erhan Bolluk, for his endless support, inspiration and contributions to my personality, since we were embryos. I would not be, who I am right now without him. I am also lucky to have tremendous friends, Murat Kurt, Barış Uyanık and Tan Narlıtepe. I have always felt their support behind me. I will always appreciate the days in Şafak 3. Also, I am thankful to have my dear friends Çağıl Cesur, İpek Bahçeci, Murat Yılmaz, Ece Demirhan, Ece Ünay and Yazın Kaçan in my life since our high school days. From the days that we were trying survive in Electrical Eng. Dept. of METU, I appreciate the friendship and influence of Efe Mucan, Ege Mahleç, Merve Salihoğlu, Emrecan Yıldırım and ,of course, Fulya Kaplan with whom I really missed spending time together.

In my last words, I would like say that I did not forget my teachers in Şahinkaya Dershanesi, they really taught a lot on science and especially I would like to thank Serhan Şahinkaya to help me establish a solid foundation in math on which I can build upon.

Hereby, I acknowledge TÜBİTAK 2211 Yurt İçi Lisansüstü Burs Programı for granting me a graduate student fellowship for my masters degree studies.

Table of Contents

1 Introduction **1**

1.1 Light field synthesized by an SLM with finite size and rectangular aperture function at Fourier plane 4

1.2 Overview of existing phase CGH algorithms 7

1.2.1 IFTA 8

1.2.2 FIDOC 10

1.2.3 Error Diffusion 11

1.3 Contributions of the thesis 19

2 Non-iterative phase hologram computation for low speckle holographic image projection **21**

2.1 Basic phase CGH computation method 21

2.2 Application to holographic image projection 26

2.2.1 Case A: Image extends over the entire CDO 27

2.2.2 Case B: Image occupies half of the CDO 33

2.3 Experimental results 34

3 High Quality Speckle Free Phase Only Computer Generated Holographic Image Projection **38**

3.1 Phase freedom on image plane in HIP 38

3.2 Basic Method - One dimensional signals 40

3.3 Two-dimensional signals 46

3.4 Simulation Results 49

3.5 Experimental results 57

4 Conclusions and Future Work 59

List of Figures

1.1 Typical optical FT architectures 4

1.2 A typical computational order of IFTA. 9

1.3 Intensity reconstructions attained at by a) 2, b)5, c)10, d)20 IFTA iterations. 10

1.4 Mean square error (MSE) convergence behavior of IFTA. 11

1.5 Intensity reconstructions attained at by a) 2, b)5, c)10 FIDOC iterations. Image/signal occupies $1/4$ of the entire diffraction order. 12

1.6 Intensity reconstructions after 10 FIDOC iterations. Image/signal occupies $25/36$ of the entire diffraction order area. 13

1.7 The coefficients used in the ED algorithm. 14

1.8 Magnitude of the frequency response of the two dimensional, discrete filter characterizing the additive error term in ED. 15

1.9 Reconstructed image by ED. Image occupies $1/9$ of the available area. 16

1.10 Reconstructed image by ED. Image occupies $1/4$ of the available area. Signal region and the error term are slightly overlapping. 17

1.11 Reconstructed image by ED. Image occupies $9/16$ of the available area. Designed error function shadows a great portion of the target image. 18

2.1 a) 2-f setup for holographic image projection (HIP) with a spatial light modulator (SLM). b) Decomposition of an arbitrary complex number $\vec{H}$ (with $|\vec{H}| \leq 2$) as the summation of two unit magnitude (phase-only) numbers $\vec{P_1}$ and $\vec{P_2}$, showing that two phase-only pixels constitute one degree of freedom. 23

2.2 Basics of the proposed phase CGH computation method. All signals are discrete. a) Desired field S. b) Ideal full-complex CGH H with two halves named H_U and H_L. c) Downsampling of S. Only even rows (rows with even index such as $k = 0, 2, \dots$) are preserved. d) Corresponding CGH, aliased as a result of downsampling. e) Downsampling of S. Only odd rows are preserved. f) Corresponding CGH. h) A phase CGH satisfying $P_U + P_L = H_U + H_L$ ($|H_U + H_L| \leq 2$), computed as in Fig. 2.1(b). g) The field generated by h. In accordance with c and d, h generates the same even rows with H. Odd rows however are left uncontrolled and appear noisy. i-j) Counterpart of g-h for perfect reconstruction of odd rows. Phase CGHs exactly control half of the degrees of freedom, as expected. 24

2.3 Verification of the basic phase CGH computation method. (a) Desired field S. Only magnitude is shown. Phase is random. (b) Magnitude of ideal full-complex CGH H. (c) Phase CGH satisfying $P_U + P_L = H_U + H_L$, shown as a gray scale image. (d) Reconstruction of c and its downsampled versions. (e) Counterpart of c-d for phase CGH satisfying $P_U - P_L = H_U - H_L$. 26

2.4 Examined HIP scenarios. (a) Desired image is specified over the entire central diffraction order (CDO). Phase freedom on the image plane is exploited to decrease encoding error. (b) Desired image is specified over half of the CDO. The unused part of CDO is reserved for encoding noise. 27

2.5 Initial phase terms (Quadratic Phase Functions - QPF) applied on the desired images to obtain a smooth energy distribution on the SLM plane. Desired image occupies (a) the entire CDO, (b) half of the CDO. In both cases, desired image is split into two parts with almost equal energies E_1 and E_2. In general, the two parts have different sizes. The upper (lower) part is mapped to upper (lower) half of the SLM via a suitable QPF term, which actually acts as a lens term that locally adjusts the ray directions for the mapping. In this way, image energy is distributed uniformly on the SLM, enabling a low encoding noise. The middle region of the SLM is left relatively empty to avoid diffraction artifacts during the calculation of phase CGHs. 31

2.6 Assignment of $\vec{P_1}$ and $\vec{P_2}$ to P_U and P_L in (a) Case A (b) Case B, where pixels on a checkerboard pattern are flipped with respect to Case A. . 31

2.7 Simulation results for *Case A*. a) Desired image specified within the entire CDO. b,c) Ideal full-complex CGHs respectively for the row and column cases, obtained by the application of the QPF terms in Fig.2.5(a). d,e) Reconstructions by phase CGHs designed respectively for even rows and even columns. Reconstructions by phase CGHs for odd rows and columns look similar. f) Time averaged reconstruction by two phase CGHs designed for even and odd rows. g) Time averaged reconstruction by two phase CGHs designed for even and odd columns. In f and g, two SLM frames are required to form each video frame. h) The average of f and g, requiring 4 SLM frames per video frame. In d and e, there are missing pixels and artifacts, hence reconstruction error is high. Note also that the artifacts in d and e appear at different locations. In f and g, information is completed, but artifacts appear persistent since only reconstructions by row or column type CGHs are averaged. In h, information is complete and artifacts are relatively suppressed, hence best image quality is achieved. 33

2.8 Simulation results of *Case B*. (a) Desired image within the CDO. Dark regions are reserved for encoding noise. (b) Corresponding ideal full-complex CGH, obtained by the application of the QPF terms in Fig.2.5(b). (c) Reconstruction by a phase CGH designed for even columns. Encoding noise mainly appears in the unused part of CDO, and odd columns within the image area appear as missing, rather than noisy, similar to that in interlaced video format. (d) Zoom-in version of c. (e) Average of the reconstructions of two phase CGHs for even and odd columns. (f) Zoom-in version of (e). In e and f, full information is restored, and speckle and encoding noise is quite low. 36

2.9 a) Experimental HIP setup. Camera is placed slightly off-axis to avoid the unmodulated beam of the SLM. b) HIP Case A, average of reconstructions of four phase CGHs. Experimental version of Fig. 2.7(f). c) HIP Case B, average of reconstructions of two phase CGHs. Experimental version of Fig. 2.8(e). The lower quality in comparison to simulation results is due to SLM pixel cross-talk and flicker effects. d) HIP Case A obtained with IFTA algorithm, which makes the speckle reduction ability of our algorithm quite evident. 37

3.1 The effect of the initial phase function imposed on a typical low-pass target image prior to the computation of a phase CGH. a) No (constant) phase results in a CGH with a strong concentration of energy that leads to a large error when magnitude information is discarded (i.e. direct quantization) to obtain a phase CGH. b) A random phase (optically equivalent to a random diffuser) leads to a CGH with a better distribution of energy and thus lower error. The shuffled nature though results in high speckle noise. c) A quadratic phase function (QPF, optically equivalent to a lens) leads to a CGH with an ordered but not necessarily uniform distibution of energy. Thus, speckle noise is suppressed, but there is still non-negligible error. d) Proposed phase term (optically equivalent to block specific lenses and prisms) that results in a CGH with an almost uniform and ordered distribution of energy (i.e. a CGH that is readily phase-only) leading to speckle-free high quality reconstructions. 41

3.2 One-dimensional simulations that verify the four cases illustrated in Fig. 3.1. a) No (constant) phase function is imposed on the target image. The magnitude of the resulting wavefield on the SLM plane is shown on the left (red curve). The dashed black rectangle indicates the SLM aperture. The reconstruction performed by the phase CGH (obtained by direct quantization) is shown on the right (red curve). The dashed black curve shows the ideal target image. b,c,d) The simulations when the phase functions applied on the target image are random, QPF and the proposed phase term, respectively. 42

3.3 The application of the proposed method in the 1D signal domain. a) Intensity of the target image. b) The associated cumulative distribution function (CDF) as computed in Eq. (3.6). c) The phase function $\phi(x)$ computed as in Eq. (3.7) (blue curve) and imposed on the target image. The red curve shows a QPF to serve as a reference, with the green curve showing the difference. d) Magnitude of the resulting wavefield on the SLM plane, that is almost uniform in the SLM aperture. e) The intensity reconstructed by the phase CGH obtained by direct quantization. 45

3.4 Illustration of the proposed method in the 2D signal domain. a) The target image is divided into rectangular blocks. An off-axis lens is imposed on each block. The lenses map the image plane to the SLM plane with a geometrical distortion that uniformizes the energy distribution. b) The rectangular image blocks are mapped into non-overlapping quadrilaterals. The area of each quadrilateral is proportional to the energy content of the associated image block. c) Target image, *Cameraman*. d) The magnitude of the CGH obtained by the designed image specific phase term. e) Reconstruction obtained with direct quantization. f) Reconstruction after 20 IFTA iterations. 50

3.5 a) Target intensity/Computed phase function $\phi(x, y)$. b) Magnitude of the CGH on SLM. c-f) Intensity reconstructions attained by 0, 2, 5 and 20 IFTA iterations, respectively. 54

3.6 Intensity reconstructions of CGHs computed by 10 IFTA iterations when the initial CGH is obtained by imposing a) random phase, b) QPF, c) proposed phase term on the target image. 55

3.7 Mean square error (MSE) convergence curves of iterated CGHs when random (blue), QPF (green) and proposed (red) phase terms are applied on the target image. 56

3.8 MSE convergence curves of iterated CGHs computed by the proposed phase terms for differently sized image blocks. $120x120$ array of blocks are used in the simulations shown in Figs. 3.5 and 3.6. 56

3.9 Experimental counterpart of Fig. 3.6. a) Random b) QPF c) proposed phase terms. The bright spot appearing on all images is due to the unmodulated beam of the SLM. 58

List of Tables

2.1 Performance of the proposed HIP algorithm for Case A. The average Mean Squared Error (MSE) and Structured Similarity Index Measure (SSIM) values of a set of desired images is reported. 32

2.2 IFTA configurations that achieve the MSE performance of the last row of Table 1. 32

3.1 Quality metrics of reconstructions shown in Fig. 3.5. 53

3.2 Quality metrics of reconstructions attained by the proposed method followed by different number of iterations. The values are averaged over a set of 8 target images. 53

3.3 Quality metrics of reconstructions attained by 10 iterations for different initial phase terms. The values are averaged over a set of 8 target images. 57

1 INTRODUCTION

Since its invention, holography has found application in various fields ranging from optical data storage, optical encryption, microscopy to neural networks [1, 2, 3]. In the early days, holograms were recorded physically by the creation of interference patterns on photosensitive materials [4]. Following the invention of computers and the development of digital signal processing tools, computer generated holography has emerged. Instead of physically recording the interference patterns, holograms generating certain desired beams and optical waves are computed digitally in a computer using scalar wave optics theory and its interpretation within signals and systems framework, Fourier optics [5].

Computer-generated holography has been an active research area for almost 60 years [6]. Computer-generated holograms (CGHs) were implemented by printed binary masks or kinoforms (photographic films) [7, 8] prior to the invention of spatial light modulators (SLMs). With the advances in the SLM technology, CGHs are now widely used in dynamic applications such as optical tweezers, beam shaping, optical information processing, optical communications, adaptive optics, wave-front correction and holographic displays [9, 10, 11, 12, 13].

Regarding display applications, holographic approach has recently become more popular due to its capability of providing all depth perception cues such as binocular disparity, convergence, accommodation, motion parallax, occlusion and blurring necessary for natural 3D experience [14]. Although the natural 3D capability seem to be the most appealing attribute of holography, it has still a lot to offer in 2D display applications, such as holographic image projection (HIP), as well.

Unlike a conventional projection system, in which a standard incoherent imaging configuration forms and projects a magnified image of a microdisplay, in a HIP system, the coherent diffraction field of a target image is calculated and displayed as a computer generated hologram (CGH) on a spatial light modulator (SLM) that is not necessarily conjugated to the projection plane; therefore enabling lensless projection, compact architectures, soft aberration correction, mechanical motion free multi-depth, light efficient infinite depth-of-focus operation [15, 16, 17, 18, 19].

However, such merits are partially shadowed due to the absence of full-complex SLMs (i.e., SLMs providing simultaneous and independent phase and amplitude control at each pixel). CGHs are ideally complex valued functions that modulate both the amplitude and phase of the incident light. Yet, available SLMs can provide only some restricted type of modulation, such as phase-only, amplitude-mostly, binary amplitude or binary phase [20, 21]. One option is to perform direct quantization on the ideal full complex CGH. This easiest option results in high levels of noise, and in general is quite sub-optimal (Yet, our method presented in Ch. 3 profoundly lowers the noise of direct phase quantization). Hence, SLM restrictions are handled via more sophisticated approaches, which can be categorized into two. In the first approach, several restricted-type SLMs are used in combination to achieve a system that provides full-complex modulation. An example is to image an amplitude-only SLM on a phase-only SLM [22]. Another is to superpose coherent beams from two phase-only SLMs [23]. A third and the most sophisticated example of such schemes, though, is proposed for binary SLMs in [24], where the authors extend the bit plane representation and decomposition of gray scale digital images to the complex valued CGH domain suggesting the use of a 4f setup for realization. However, such methods have complicated optical setups and require high precision (nm scale) alignment. They thus have limited utility.

The second approach encodes the ideal full-complex CGH into a restricted type CGH that can be displayed on the SLM. As a result of the encoding process, the SLM output consists of a noise beam along with the desired beam. The encoding procedures are usually tuned so that the noise beam has reduced energy, or gets spatially separated from the desired beam in the course of propagation. Many algorithms are proposed for various SLM types. [25, 26] investigate the CGH computation for amplitude-only and amplitude mostly SLMs, while [27, 28] explore the binary SLM case.

Among currently available SLM types, phase-only liquid crystal-on-silicon (LCoS) SLMs constitute the most attractive option for HIP with their small pixel pitch, high pixel count, relatively high diffraction efficiency and 8-bit modulation depth [19, 21]. Yet, their restricted (phase-only) modulation capability leads to limited image quality, which is further degraded by speckle noise resulting from the coherent nature of illumination light [29]. In this respect, performance of phase CGH computation algorithms are of crucial importance. Research presented in [30, 31, 32, 33, 34, 35] establishes some of the examples of effort put to devise an optimum phase CGH algorithm. In general, these algorithms perform successful encodings. However, almost all of them have an iterative structure and involve repetitive Fast Fourier Transform (FFT) or pixel-by-pixel processing operations that pose significant computational complexity. In spite of the improvements in the computational power and parallel processing hardware such as FPGAs and GPUs, real-time operations still remain as a challenge due to lack of non-iterative direct solutions.

Another disadvantage of most established phase CGH computation algorithms, especially in the HIP context, is related to speckle noise. As well known, all laser based display systems are prone to speckle noise to some degree [29]. In HIP, speckle partly results due to physical factors such as the surface roughness of optical components or projection screens, and partly due to the CGH computation procedure. In particular, most algorithms converge to a solution by assigning random phase values to the desired image samples, leading to speckled reconstructions even if physical factors of speckle are removed. Some algorithms limit the phase variation during iterations to achieve speckle reduction, but at the cost of slower convergence and increased computational cost [36].

During the research underlying the methods and ideas presented in this thesis, we challenged ourselves to devise phase CGH computation algorithms that contribute to existing literature in the sense that while our methods are decreasing the computational complexity compared to the previous works, they also attain higher reconstruction quality without compromising from light efficiency and/or field-of-view (FOV) of the overall system. Therefore, this thesis can be seen as an investigation towards understanding the fundamental limits of phase-only computer holography in the context image projection.

Before digging into the details of the presented research, we develop mathematical closed form for the light synthesized by an SLM in Section 1.1. In Section 1.2, we will have a more detailed discussion concerning the phase CGH computation algorithms previously published in the literature. Section 1.3 is reserved for contribution statement of the thesis.

1.1 Light field synthesized by an SLM with finite size and rectangular aperture function at Fourier plane

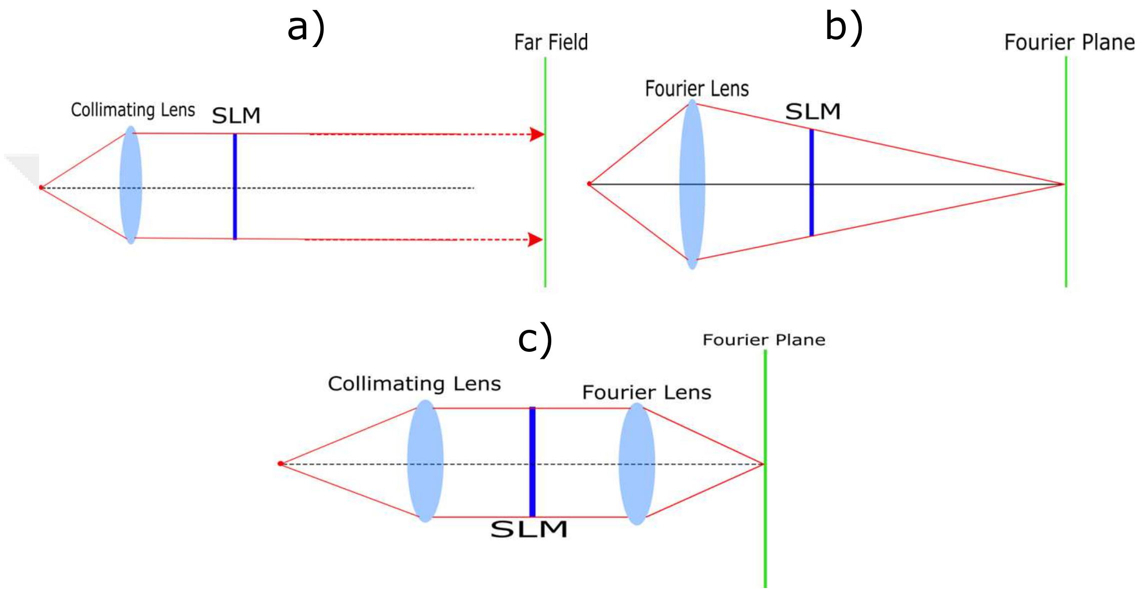

Figure 1.1. Typical optical FT architectures

Most of the SLMs today have pixellated nature and among these the pixels are in general have rectangular aperture functions. The typical values range from 40 μ m to recently reported 3.74 μ m. Even though 3.74 μ m is the smallest reported pixel pitch until now, it is still a large aperture size compared to the wavelength of visible light, $\lambda \in (400, 700)$ nm. Thus, in HIP applications it is mostly assumed that the practical image sizes are attained at distances where Fresnel diffraction assumption is valid.

Another thing to note for the sake of discussion is the fact computing a phase computer generated hologram for an image at Fourier plane or at a plane inside Fresnel or fractional Fourier zone does not differ much. Since the propagation kernels between planes related by Fresnel or fractional Fourier Transforms are based on regular Fourier Transform (FT) and pre and/or post pure phase function multiplications, thus such multiplicative terms can be handled trivially in the case of a phase SLM. Therefore, we keep our discussion limited to the case where the image plane and the SLM plane are related by FT under appropriate definition of frequency and space variables (typical optical architectures that can be examined by FT relation is shown in Fig. 1.1).

In this section, we will analyze the light field synthesized by a finite size SLM with rectangular pixel aperture, but we will not impose any constraints on the SLM pixel values yet. To begin with, it needs to be stated that SLMs are usually modeled as $2D$ thin optical masks. In the context of scalar wave optics theory, a thin optical mask with $2D$ complex transmittance, $t(x, y)$, is represented as a multiplicative element. In other words, if the mask is placed at $z = 0$ and illuminated by a wave from the left hand side whose profile is $w_{0-}(x, y)$ then the optical wave leaving the mask, $w_{0+}(x, y)$, can written as $w_{0+}(x, y) = w_{0-}(x, y)t(x, y)$. Although the view of SLM described in this model is only an approximation, it is sufficient for our purposes, hence it will be used throughout this thesis.

Particularly, we will analyze the light field generated by SLM for the optical setup depicted in Fig. 1.1(c). At this point, let us make the following definitions;

- f denotes the focal length of the Fourier lens,
- Δ_X and Δ_Y denote the SLM pixel pitch in respective directions,
- SLM has $M \times N$ pixels.

Let SLM is illuminated by a uniform plane wave as shown in Fig. 1.1(c) ($w_{0-}(x, y) = 1$). Then the wave profile at a plane just after the SLM is given by $w_{0+}(x, y) = h(x, y)$ where $h(x, y)$ denotes the transmittance function on SLM (For now, there is no restriction on the values that $h(x, y)$ can take).

It is well known that the optical field to be observed on the right focal plane (x', y'), of the Fourier lens, $g(u, v)$, is exactly the Fourier Transform (FT) of $h(x, y)$ with coordinate scaling factors $(u = x'/\lambda f), v = y'/\lambda f))$ as in Equation (1.1) (Note that finite size of the Fourier lens is neglected). Since we compute the CGH samples digitally on computer, first we need to write $h(x, y)$ in terms of those computed samples $s[m, n]$ to fully understand the properties of $g(u, v)$.

$$g(u, v) = \int_{-\infty}^{\infty} \int_{-\infty}^{\infty} h(x, y) e^{(-j2\pi(ux+vy))} dx\, dy \tag{1.1}$$

Starting by the conversion of sequence $s[m,n]$ (discrete function) to its continuous counterpart $s(x,y)$, we get

$$s(x,y) = \sum_{m=-\infty}^{\infty} \sum_{n=-\infty}^{\infty} s[m,n]\delta(x - x_m, y - y_N) \tag{1.2}$$

where $x_m = m\Delta_X$, $y_n = n\Delta_Y$ denote the pixel positions for an SLM placed symmetric around the origin. Notice that $s(x,y)$ represents the continuous transmittance of an SLM with impulsive pixels.

Incorporating the interpolation, Equation (1.2) becomes,

$$h(x,y) = [a(x,y) \ ** \ s(x,y)] \, rect\left(\frac{x}{M\Delta_X}\right) rect\left(\frac{y}{N\Delta_Y}\right). \tag{1.3}$$

where $**$ denotes 2D convolution operation, $a(x,y)$ is the pixel aperture function of SLM and $rect\left(\frac{x}{M\Delta_X}\right) rect\left(\frac{y}{N\Delta_Y}\right)$ determines the finite size of SLM.

Note that, $a(x,y) = rect(\frac{x}{\Delta_X})rect(\frac{y}{\Delta_Y})$ for an SLM with rectangular pixels. Placing that into Equation (1.3) and then taking the FT as defined in Equation (1.1), we arrive,

$$\begin{aligned} g(x',y') = &\left[sinc(\frac{x'}{\lambda f}\Delta_X)sinc(\frac{x'}{\lambda f}\Delta_Y)\mathcal{F}(s(x,y))\right] \\ &** \, sinc\left(\frac{x'}{\lambda f}M\Delta_X\right) sinc\left(\frac{y'}{\lambda f}N\Delta_Y\right). \end{aligned} \tag{1.4}$$

where $\mathcal{F}(\cdot)$ represents the FT (Note that in Equation (1.4) constant normalization terms that must appear under unitary transform condition are ignored).

We will examine Equation (1.4) under the view that an SLM with pixel size (Δ_X, Δ_Y) will create diffraction orders separated by $\lambda f/\Delta_X$ and $\lambda f/\Delta_Y$ in each direction. The region around the origin at Fourier plane described by $x' \in (-\lambda f/(2\Delta_X), \lambda f/(2\Delta_X)$ and $y' \in (-\lambda f/(2\Delta_Y), \lambda f/(2\Delta_Y)$ is called the Central Diffraction Order (CDO). Since the higher orders of the SLM does not contain any additional information, we are only interested in designing the CDO accordingly.

A closer look to Equation (1.4) reveals that the multiplicative $sinc$ factors coming from the rectangular aperture function are wide enough (due to relatively small pixel pitch) so that inside the CDO their effect can be modeled as multiplicative constant [37]. However, the $sinc$ convolution representing the finite SLM aperture cannot be discarded, since it plays a vital role in the formation of high frequency noise terms, such as speckle, on the reconstruction. Therefore, the simulation results provided throughout this thesis, assumes impulsive pixels on SLM side; on the other hand, they take the effect of finite SLM aperture into account.

1.2 Overview of existing phase CGH algorithms

Many different algorithm have been proposed for the computation of phase diffractive optical elements (DOEs) and CGHs. To be more precise, here is a list of most widely used methods;

- Iterative Fourier Transform Algorithm (IFTA) [32, 33, 34, 36, 38]
- Gerchberg-Saxton Algorithm (GS) [39, 40]
- Fresnel Ping-Pong [41]
- Fienup with Don't Care (FIDOC) [16, 31, 42]
- Error Diffusion [30, 43, 44, 45]
- Minimum Average Error Algorithm [46, 47, 48]
- Simulated Annealing [49]
- Direct Search [27, 50]
- Conjugate Gradient [51]
- Double Phase Hologram [52]

From the list above, IFTA, GS, Fresnel Ping-Pong and FIDOC can be taken into one group considering their mathematical basis. These algorithms are generally known as projection onto sets type optimization methods. They are often used in convex optimization problems and when the two sets are convex, it is called Projection Onto Convex Sets (POCS). Unfortunately, the performance of such algorithms is only limited in phase CGH computation mainly due to the fact that phase-only set of values on the SLM plane do not constitute a convex set [53]. FIDOC distinguishes itself from the others in the sense that IFTA and GS algorithms are essentially phase retrieval methods but FIDOC defines a procedure specifically for the design of phase holograms which will be explained further in Section 1.2.2.

From the implementation perspective, error diffusion (ED), minimum average error (MAE), simulated annealing, direct search (DS) and double phase hologram algorithms are based on pixel-by-pixel processing of the full-complex CGH. Double phase hologram method defines macro-pixel concept which is composed of two phase-only neighboring pixels of the SLM. But the region which can be addressed with high quality using that procedure is very limited on the image plane so it is seldom used [54].

On the other hand, DS and simulated annealing methods impose substantially high computational load but in return they generally produce high quality reconstructions. Due to their high computational complexity, they find application in DOE designs, which is not a dynamic element, rather than systems requiring real-time computation.

The equivalence of ED and MAE algorithms is stated in [48], since ED has been found to perform slightly better and found application in a greater volume, it is going to be discussed further in 1.2.3.

1.2.1 IFTA

Fig. 1.2 illustrates a typical computational cycle of IFTA. In general, IFTA and GS algorithms have become popular since they allow the Fast Fourier Transform (FFT) algorithm to be utilized during computation. From Fig. 1.2, it is clear that the implementation relies on enforcing the constraints on both image and SLM planes, back and forth. However, due to their impractically slow convergence behavior, their performance regarding the final image quality is only moderate. Fig. 1.3(a-d) show typical outcome of 2, 5, 10, 20 IFTA iterations performed on a CGH to reconstruct a gray

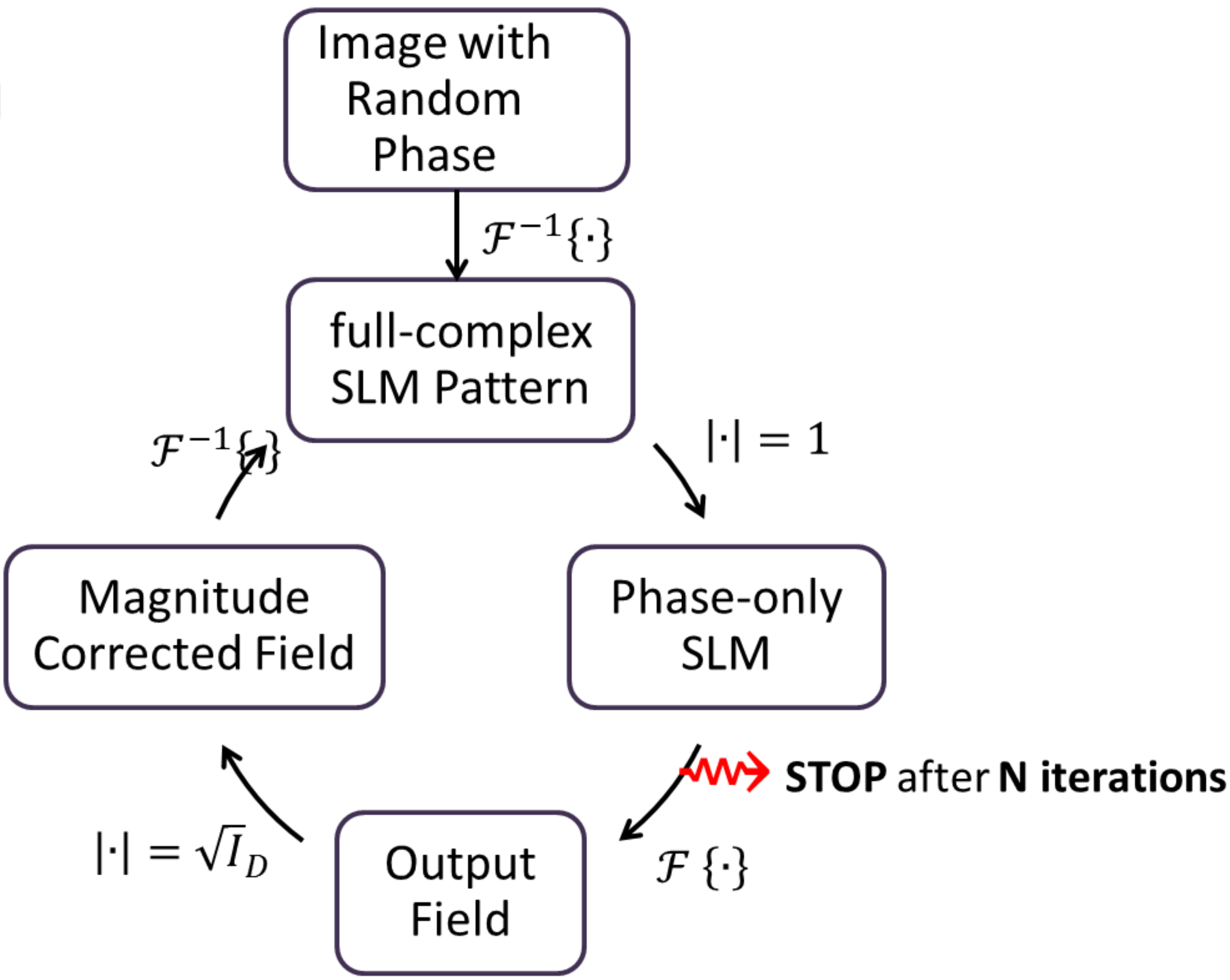

Figure 1.2. A typical computational order of IFTA.

scale target image, *Lena*, respectively. Additionally, MSE convergence curve attained by the trials performed on 10 different gray scale images is depicted in Fig. 1.4.

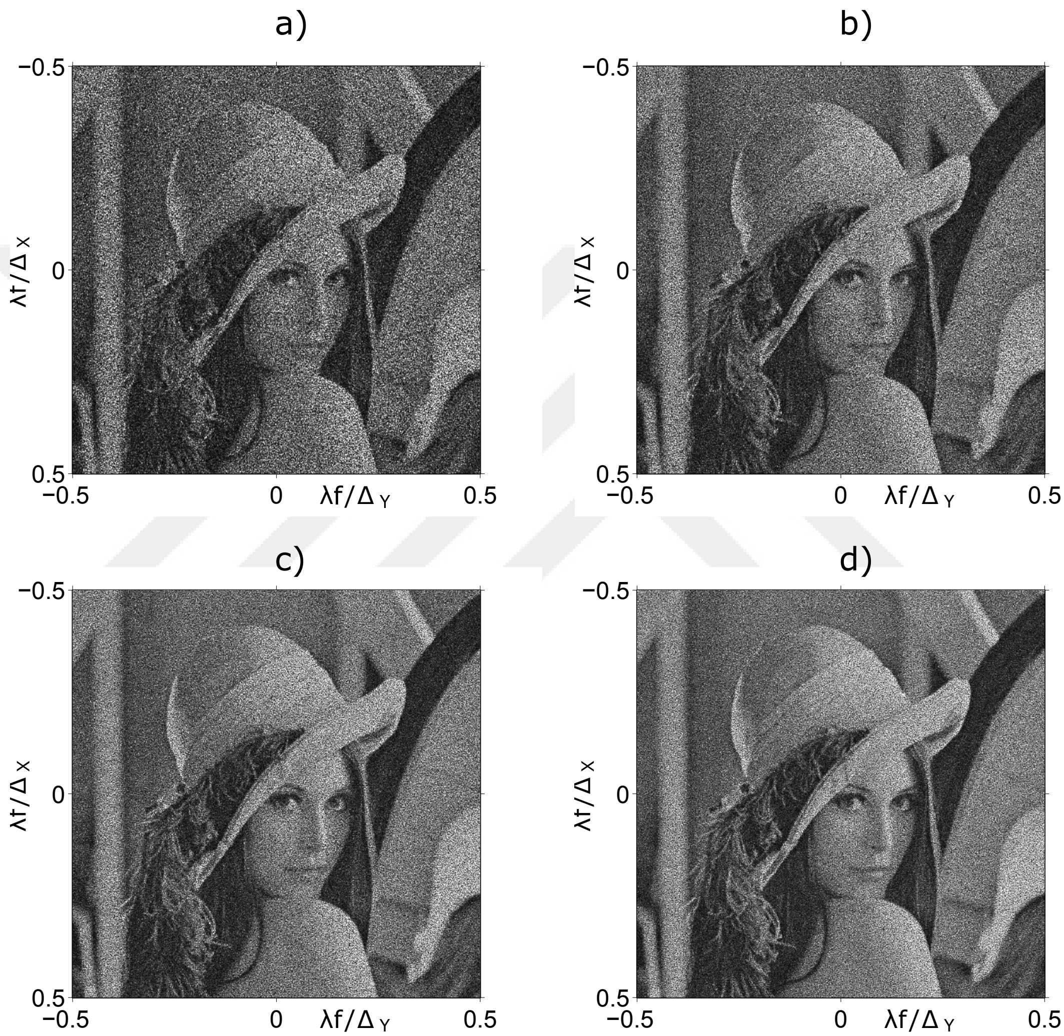

Figure 1.3. Intensity reconstructions attained at by a) 2, b)5, c)10, d)20 IFTA iterations.

1.2.2 FIDOC

The idea of leaving dummy or 'Don't care' areas in a diffraction order of SLM to ease the convergence of iterative algorithms was first introduced by Akahori et. al. [42]. Then it was further improved by assigning amplitude freedom over some parts of the image region as well in [31]. The underlying key observation on both articles was the fact that Fienup/IFTA/GS type algorithms are essentially designed to solve phase

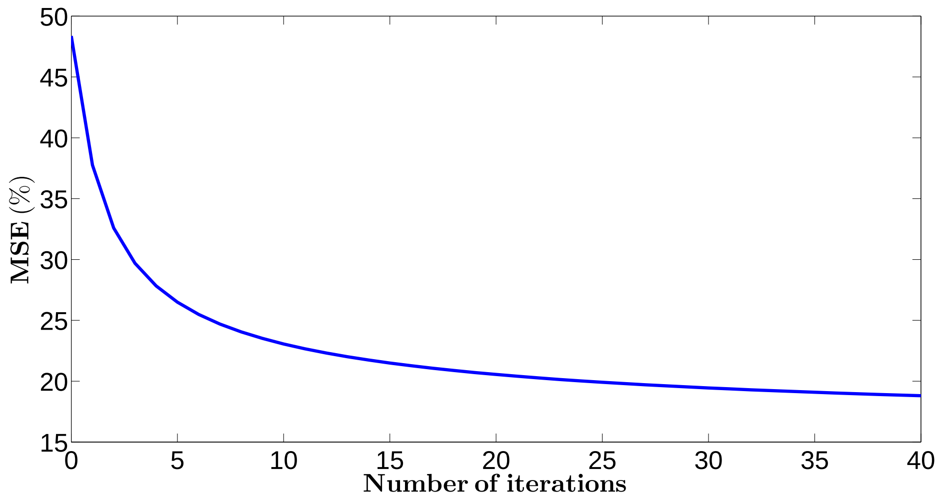

Figure 1.4. Mean square error (MSE) convergence behavior of IFTA.

retrieval problem; however, phase cGH computation can be interpreted also from the design perspective instead of information retrieval.

The main difference between IFTA and FIDOC lies beneath the constraints applied on the image plane during iterations. While the amplitude of the ideal wave field at image plane is forced for the entire diffraction order in IFTA, FIDOC only imposes the ideal amplitude and phase information onto a limited region which can be viewed as signal window. Thereby, the convergence is substantially quicker and since the phase information inside the signal window is also reconstructed, the speckle effect might be reduced significantly as illustrated in Fig. 1.5. As the quicker convergence and relatively high quality of reconstructions are the favorable attributes of FIDOC, it limits the attainable image size/FOV and the light efficiency. For instance, when it is desired to enlarge the image area as in Fig. 1.6, the algorithm does not converge and thus can not reconstruct the desired gray levels.

1.2.3 Error Diffusion

Floyd and Steinberg introduced the ED algorithm (also known as Floyd-Steinberg dithering) for halftoning of the gray scale images [45]. Yet, it has found application in CGH domain as well.

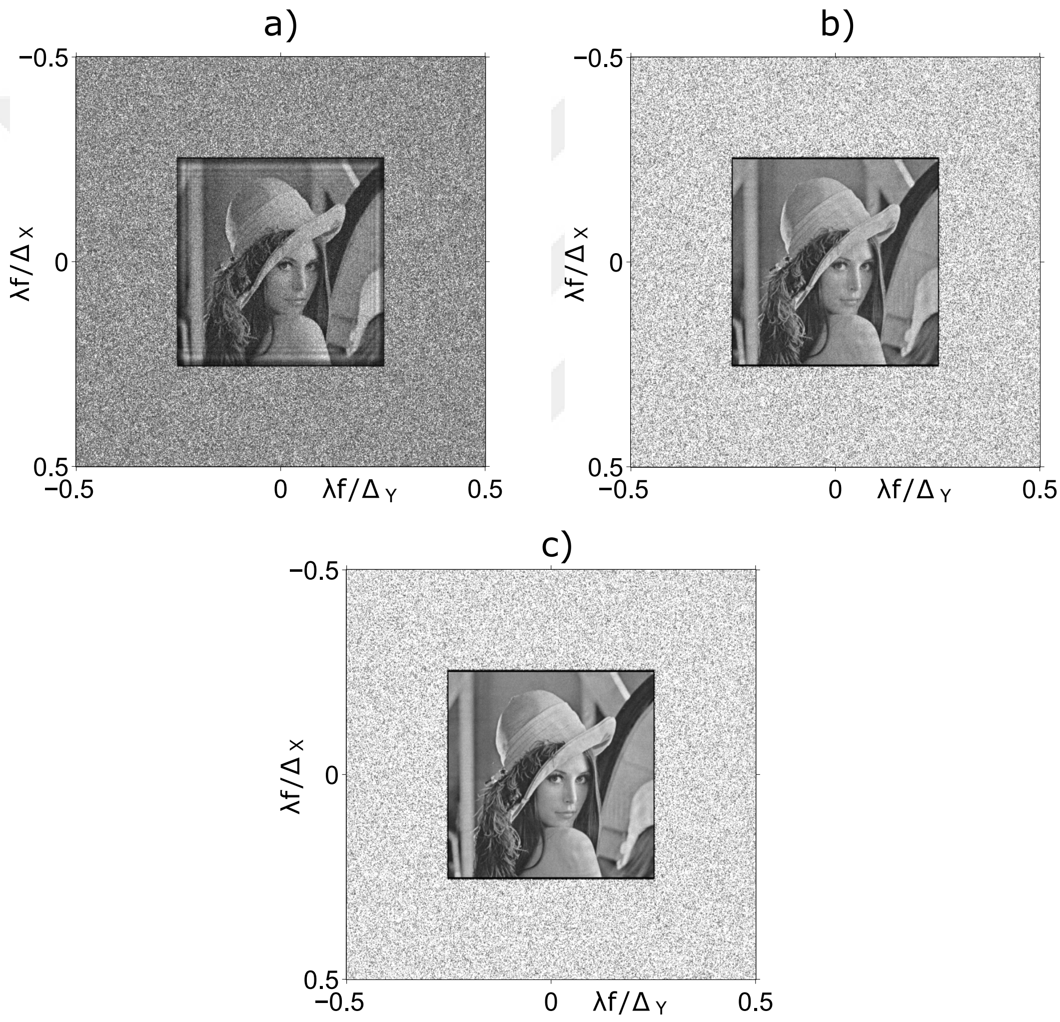

Figure 1.5. Intensity reconstructions attained at by a) 2, b)5, c)10 FIDOC iterations. Image/signal occupies $1/4$ of the entire diffraction order.

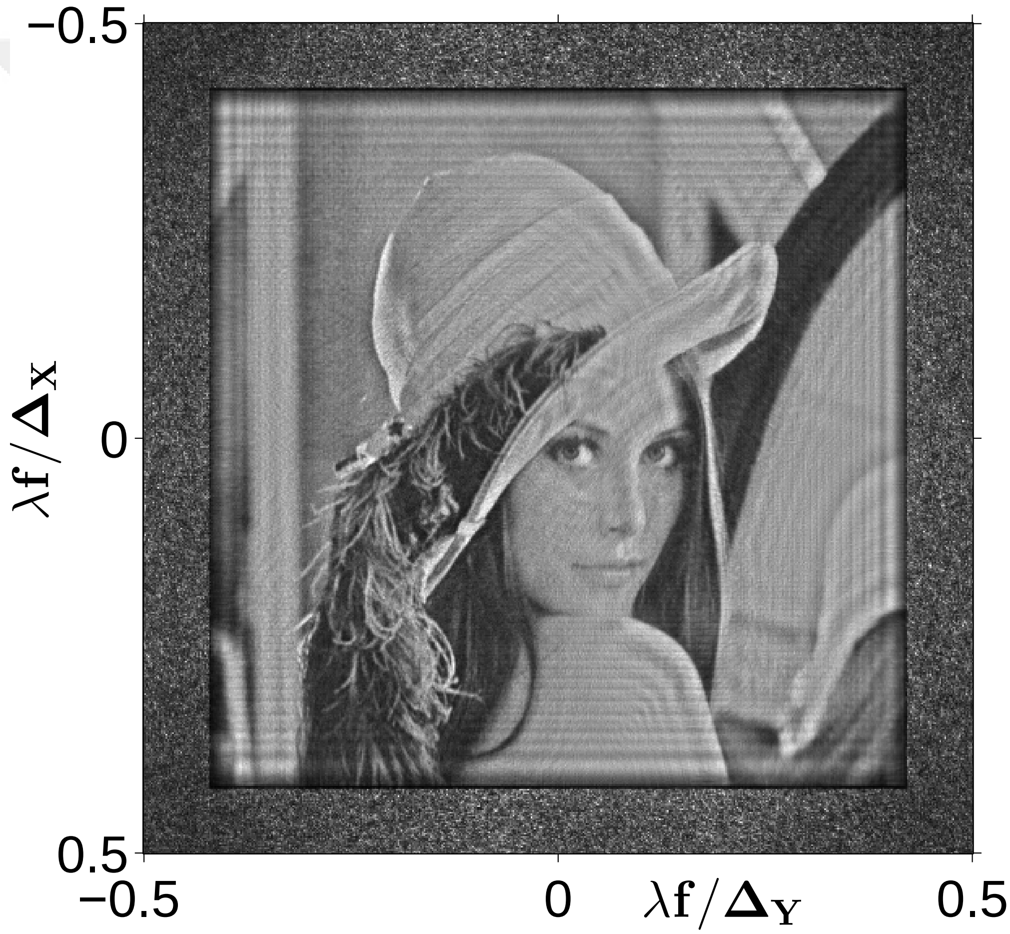

Figure 1.6. Intensity reconstructions after 10 FIDOC iterations. Image/signal occupies $25/36$ of the entire diffraction order area.

If we call our full-complex, ideal CGH samples as $h(m,n)$, then ED basically models an additive error term, $e(m,n)$, through pixel-by-pixel processing of $h(x,y)$ such that $h(m,n)+e(m,n)=p(m,n)$ where $p(m,n)$ is a phase-only function. In addition, $e(m,n)$ is designed such that it does not affect the low frequency region in the Fourier domain i.e., it has a high pass nature. Figs. 1.7 and 1.8 show the coefficients as they were defined by [45] and magnitude of the associated frequency response of the $2D$, discrete filter described by these coefficients, respectively. Since the first introduction of the algorithm, different versions with 8, 16 and 32 coefficients have been proposed but the improvement compared to the original form in Fig. 1.7 was only minor[47].

Even though, ED performs successful phase-only encoding, it compromises from the FOV and light efficiency similar to FIDOC. Moreover, since it is based on pixel-by-pixel processing, as the pixel count of the modern day SLMs gets larger, the computational burden of the algorithm becomes even harder to tackle for real-time applications.

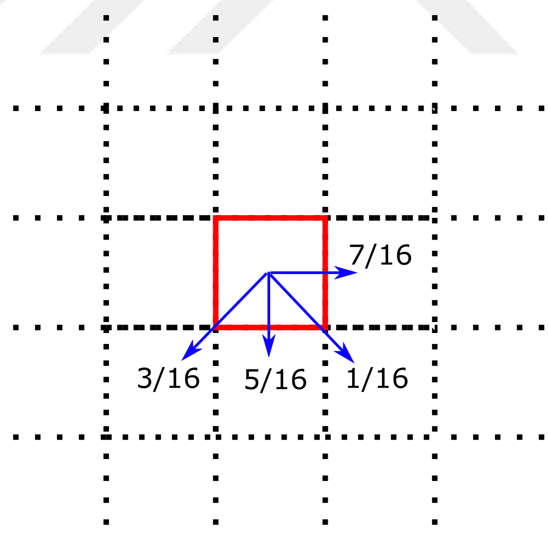

Figure 1.7. The coefficients used in the ED algorithm.

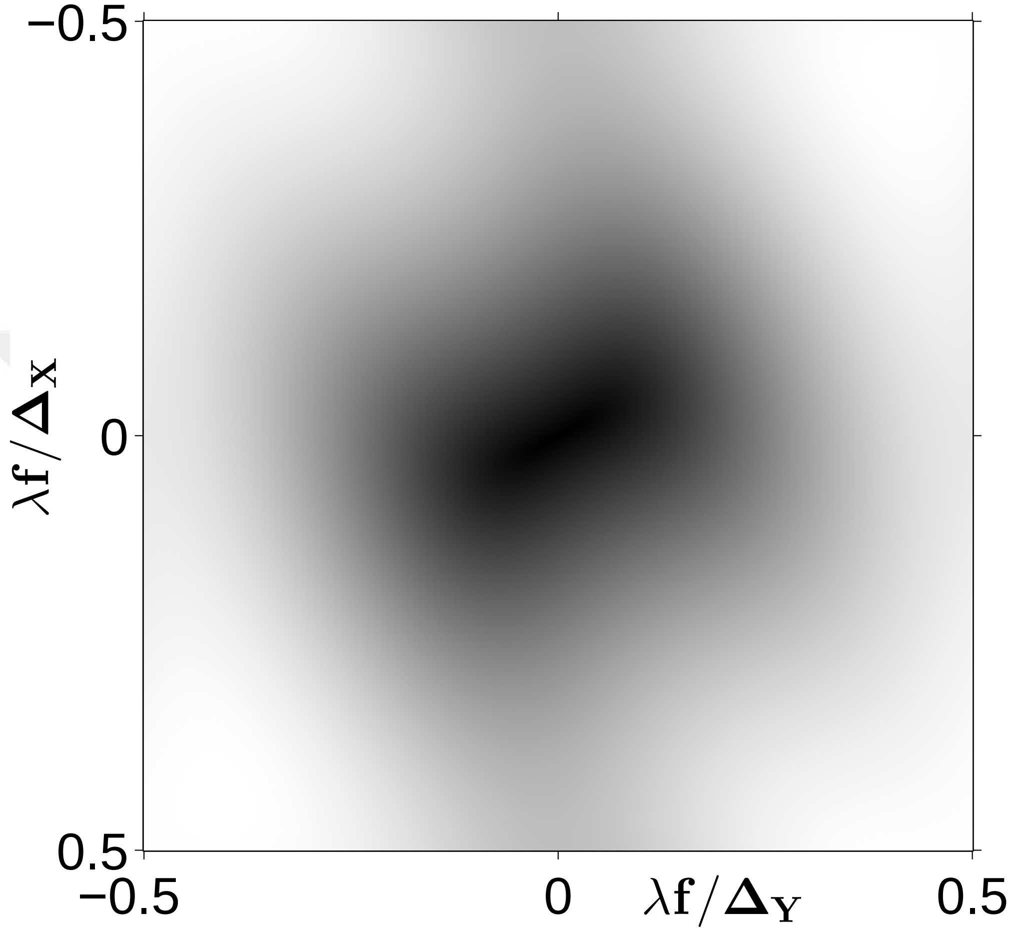

Figure 1.8. Magnitude of the frequency response of the two dimensional, discrete filter characterizing the additive error term in ED.

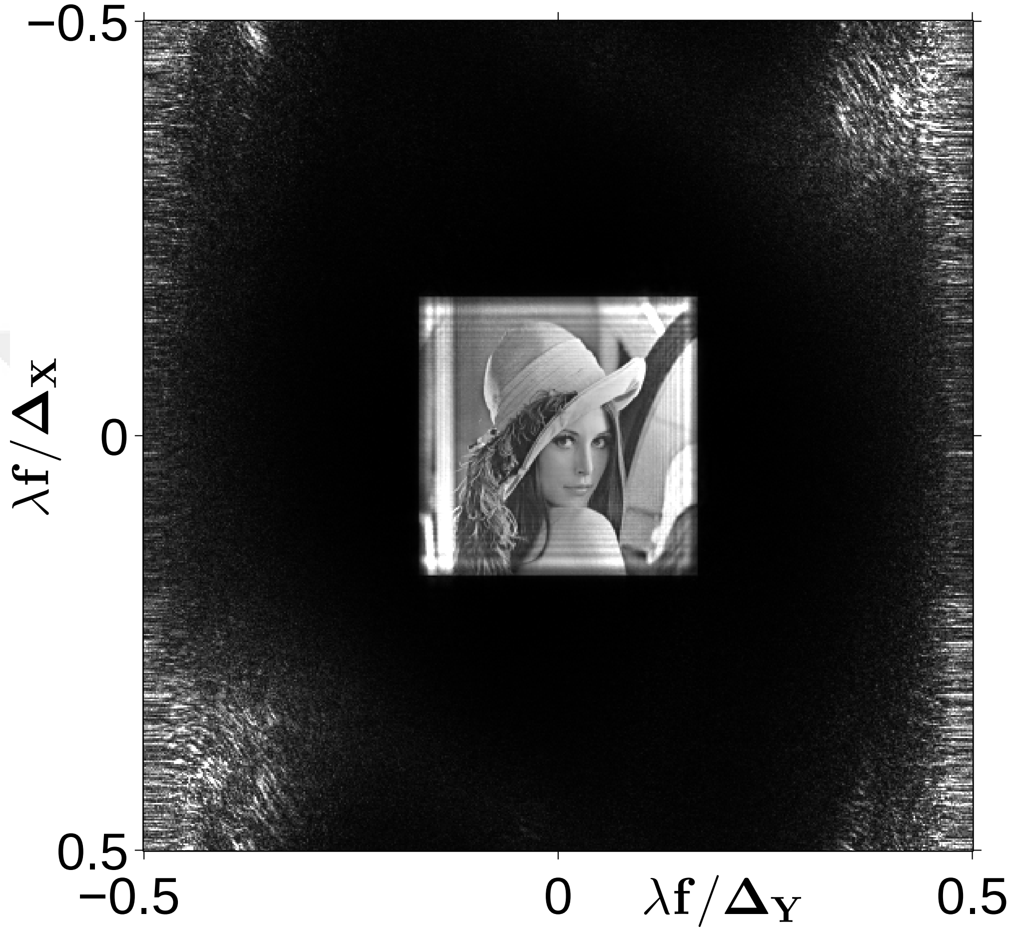

Figure 1.9. Reconstructed image by ED. Image occupies $1/9$ of the available area.

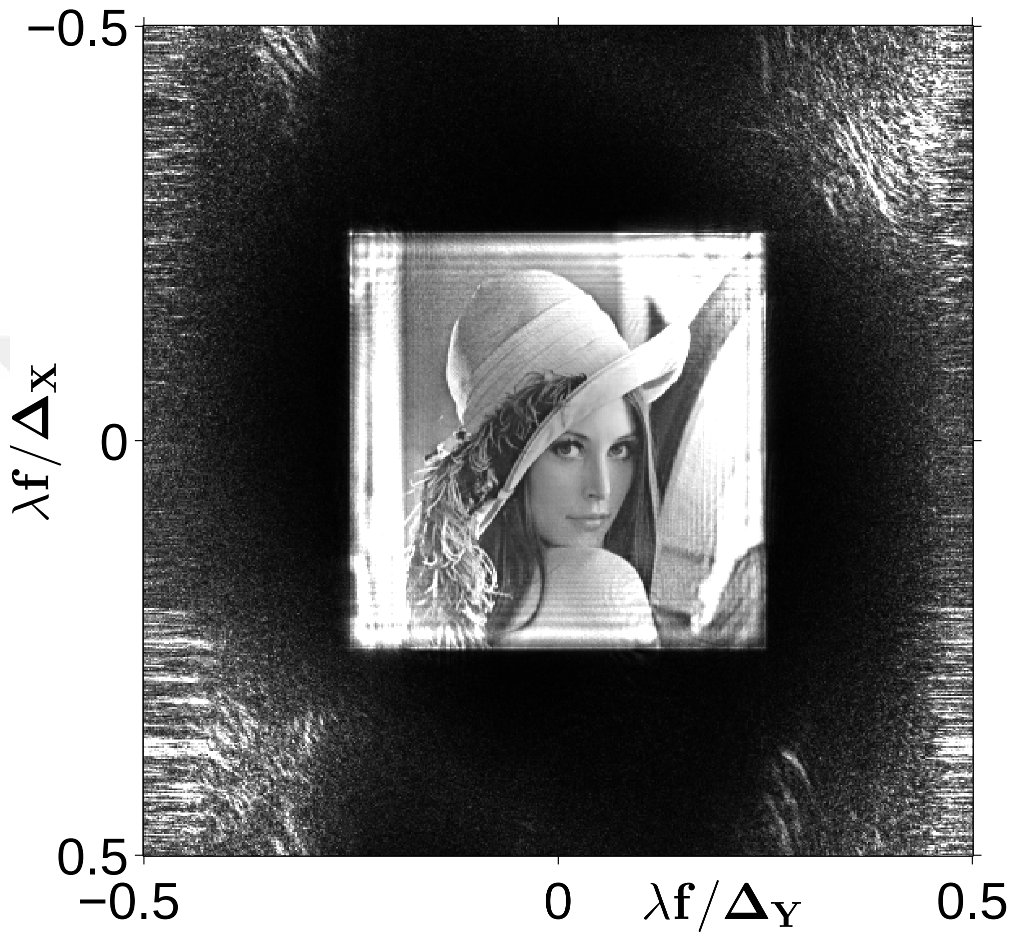

Figure 1.10. Reconstructed image by ED. Image occupies $1/4$ of the available area. Signal region and the error term are slightly overlapping.

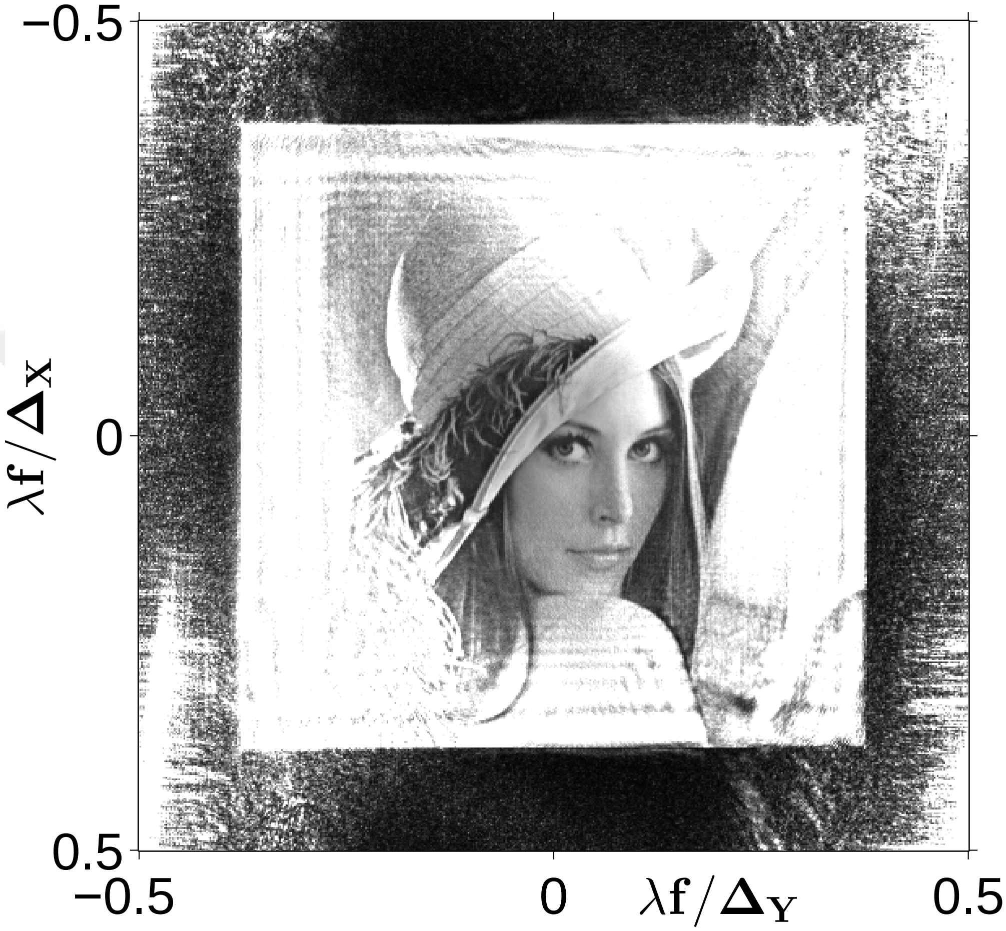

Figure 1.11. Reconstructed image by ED. Image occupies $9/16$ of the available area. Designed error function shadows a great portion of the target image.

1.3 Contributions of the thesis

This thesis reports a novel phase-only CGH encoding algorithm in the first part. The novelty of the devised algorithm lies beneath its computational advantages. It is the first time that a non-iterative phase CGH encoding algorithm which can generate high quality images (MSE 3%) is reported. With the already available 60Hz phase-only SLM technology, it is possible to compute the CGHs in real-time which generate high quality, speckle free holographic video frames in the interlaced format. When the FOV and/or the power efficiency of the HIP system are important design parameters, then the proposed algorithm requires higher frame rates (240Hz) for high quality images (MSE 12%).

In the second part, an image specific phase design is presented. The research of this phase function is explicitly carried out to overcome the trade-off between the image size and image quality in the existing literature. Previous to this work, either images occupying whole diffraction order can be reconstructed with speckle, thus with poor quality or the image size kept smaller so that there are regions in the diffraction order reserved for the encoding noise to be thrown. The proposed phase design constitutes the basis for the computation of phase CGHs which can reconstruct speckle free, high quality images without compromising from their size inside a diffraction order as well as the power efficiency of the overall HIP system. It is the first time that such phase CGHs are reported in the HIP literature.

Although the experiments carried out during this thesis are kept at the proof-of-concept level, two major problems associated with the holographic displays using phase SLMs are addressed and solutions with theoretical basis are provided. The methods in this thesis can be used in any holographic display platform if the underlying assumptions are satisfied and optical architecture is appropriate. For instance, in the wide FOV near-to-eye display project carried in OML, the second method can be used to project images which are going to be relayed to the retina by the help of an additional optical component such as an elliptical mirror. The necessity of aberration correction at some level is going to be needed in such a scenario but once the profile of aberrations is studied specifically for that relay optics, it is fairly straightforward to adjust the phase CGHs. Moreover, since the two investigated aspects of phase

CGH computation complement each other, they can also be used in combination in the following order. First the initial phase design is performed for a specified image and then the ideal, full-complex CGH can be encoded into a phase-only one via the algorithm presented in the first part. Since the proposed phase design results in ideal, full-complex CGHs to have magnitude distributions already as uniformly as possible, the image quality performance of the encoding algorithm is going to be improved (Ghost image artifacts suffered by images shown in Fig. 2.7 is going to be reduced).

Additionally, during the research reported in this thesis, one conference paper at Digital Holography&3D Imaging Conference and one journal article at Optics Express, OSA has been published. A second journal article has been drafted [55, 56].

2 NON-ITERATIVE PHASE HOLOGRAM COMPUTATION FOR LOW SPECKLE HOLOGRAPHIC IMAGE PROJECTION

In this chapter, we present a non-iterative phase CGH computation algorithm which is particularly suitable for real-time HIP applications. In Section 2.1, we describe a basic method, which is first presented in [55]. With this method, we can compute phase CGHs whose discrete Fourier transforms (DFTs) are exactly controlled on half of the samples, such as even (or odd) indexed rows (or columns). The method requires only a single FFT and trivial arithmetic operations. In Section 2.2, we supplement the basic method by the application of structured non-random initial phase terms on a desired image. In this way, we reduce encoding noise while keeping speckle noise low and get high quality reconstructions under temporal averaging. Section 2.3 shows the experimental results with a commercially available phase-only SLM.

2.1 Basic phase CGH computation method

We assume that images are projected at a Fourier plane of the SLM, hence the field distributions on the hologram and the output planes are related by a Fourier Transform (FT). We present the analysis for the 2-f setup shown in Fig. 2.1(a). Extensions to other FT configurations are straightforward. The SLM (assumed to be pixellated) is placed at the left focal (hologram) plane and is illuminated with a normally incident plane wave. The pixel values of the SLM are denoted by $H_{m,n}$. The resulting analog field on the right focal (output) plane is denoted by $s(x, y)$. Due to the pixellated nature of SLM, $s(x, y)$ is periodic (under the assumptions of impulsive pixels and Fresnel diffraction) with periods $\frac{\lambda f}{\Delta_x} \times \frac{\lambda f}{\Delta_y}$, where f denotes the focal length of the Fourier lens, λ denotes the wavelength and Δ_x, Δ_y denote the SLM pixel periods in x and y directions, respectively. $s(x, y)$ can be uniquely controlled over only one period, which we call the central diffraction order (CDO). The remaining regions of the output plane merely consist of higher order replicas of the CDO with no additional information. If the SLM has $M \times N$ pixels, $s(x, y)$ is also completely specified by its $M \times N$ samples taken within the CDO, with intervals $\frac{\lambda f}{M\Delta_x}, \frac{\lambda f}{N\Delta_y}$. Letting $S_{k,l}$ denote these samples, we have

$$S_{k,l} = \mathbf{DFT}\{H_{m,n}\}. \tag{2.1}$$

From now on, we drop the index subscripts, hence H denotes the SLM pixel values and S denotes the samples of the output field within the CDO.

For an arbitrary S, H is in general full complex. Thus, if we had a full-complex SLM with a very high dynamic range, we could fully reconstruct any given S. In case of a phase-only SLM though, we in general can not reconstruct S fully. However, a phase-only SLM should be able to (and indeed can) control (reconstruct) $MN/2$ samples of S exactly. This follows from the well-known fact that a complex number $\vec{H}$ with $|\vec{H}| \leq 2$ can be expressed as the summation of two unit magnitude complex numbers [52], i.e., $\vec{H} = \vec{P_1} + \vec{P_2}$ where $|\vec{P_1}| = |\vec{P_2}| = 1$, as shown in Fig. 2.1(b). In particular, $\vec{P_1}$ and $\vec{P_2}$ can be found as

$$\vec{P_1} = e^{j(\angle\vec{H} - \alpha)} \tag{2.2a}$$

$$\vec{P_2} = e^{j(\angle\vec{H} + \alpha)} \tag{2.2b}$$

where

$$\alpha = \arccos(\frac{|\vec{H}|}{2}). \tag{2.3}$$

Thus, two phase-only pixels of the SLM together constitute one degree of freedom, yielding a total of $MN/2$ degrees of freedom, which should be sufficient for controlling half of S.

We now determine which $MN/2$ samples of S should be targeted. Our concern is that the phase CGH that reconstructs the chosen samples should be determined in a direct manner without any iterations. Figure 2.2 illustrates our methodology. Figure 2.2(a) shows a desired S as an $M \times N$ discrete image. Figure 2.2(b) shows the ideal full-complex $M \times N$ CGH H that generates S. In Fig. 2.2(b), the upper and lower parts of H are labeled as H_U and H_L, respectively. Both H_U and H_L are $M/2 \times N$

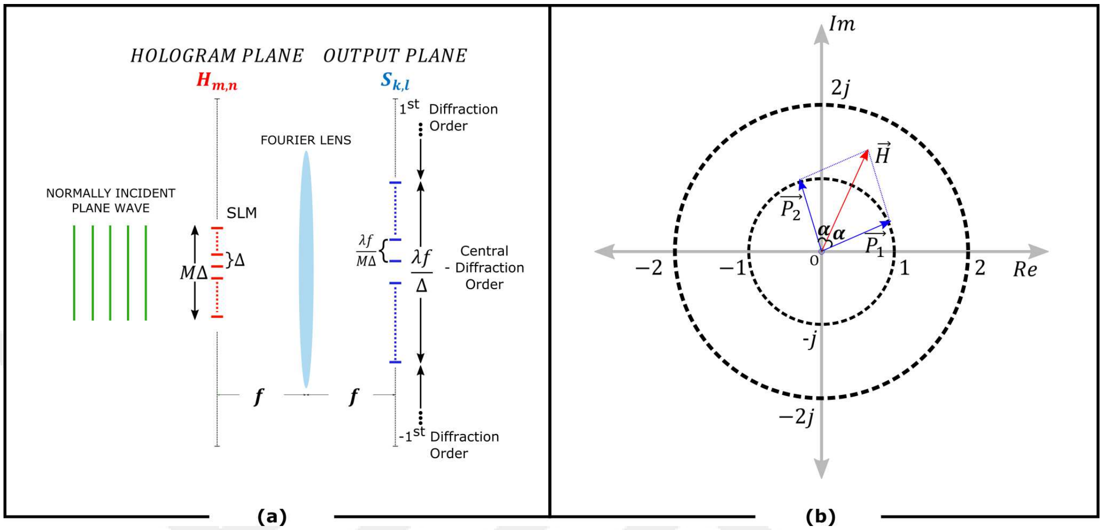

Figure 2.1. a) 2-f setup for holographic image projection (HIP) with a spatial light modulator (SLM). b) Decomposition of an arbitrary complex number $\vec{H}$ (with $|\vec{H}| \leq 2$) as the summation of two unit magnitude (phase-only) numbers $\vec{P_1}$ and $\vec{P_2}$, showing that two phase-only pixels constitute one degree of freedom.

patterns. Next, in Fig. 2.2(c), S is downsampled such that only the even rows (i.e., rows with even indexes such as $k = 0, 2, 4, \dots$) are preserved and odd rows are zeroed. This downsampling as well-known implies aliasing in the Inverse DFT domain, as illustrated in Fig. 2.2(d). In particular, upper and lower parts of H are overlapped and superposed. Conversely, the CGH in Fig. 2.2(d) is the CGH that generates the output samples in Fig. 2.2(c). Thus, when only the even rows of S are of concern, it is $H_U + H_L$ that matters, and the individual H_U and H_L does not matter. Figure 2.2(e) and Fig. 2.2(f) illustrate the dual case of downsampling of odd rows, and show that when odd rows of S are of concern, it is only $H_U - H_L$ that matters. Here, H_L is weighted with a negative coefficient as a result of the one unit downward shift of the impulse train in Fig. 2.2(e). Finally, Fig. 2.2(h) shows an $M \times N$ phase CGH which satisfies the condition $P_U + P_L = H_U + H_L$. Here, we assume that $|H_U + H_L| \leq 2$ (which can be achieved with a trivial normalization of H). For each pixel of $H_U + H_L$, we can find $\vec{P_1}$ and $\vec{P_2}$ according to Eqs. (2.2) and (2.3). Then we can set one of P_U, P_L to $\vec{P_1}$ and the other to $\vec{P_2}$. By Fig. 2.2(c) and Fig. 2.2(d), the phase CGH in Fig. 2.2(h) reconstructs the same even rows with H, as in Fig. 2.2(g). Hence, if the target samples are chosen as the samples on even rows, they can be exactly controlled via a phase CGH computed without any iterations. Note also that although the phase CGH in Fig. 2.2(h) reconstructs even rows of S exactly, it in general does not reconstruct the odd rows because $P_U - P_L$ is not necessarily equal to $H_U - H_L$. Indeed, in general, one can select P_U and P_L to satisfy either of the conditions $P_U + P_L = H_U + H_L$ or $P_U - P_L = H_U - H_L$, but not both. Hence, odd rows in Fig. 2.2(g) are set in an uncontrolled manner, and the reconstruction is degraded by a noise term given by $(H_U - H_L) - (P_U - P_L)$. Figure 2.2(i) and Fig. 2.2(j) show the case where the phase CGH perfectly reconstructs odd rows and leaves even rows noisy. In a straightforward manner, the idea can be extended to perfectly reconstruct even or odd columns. In this case, CGHs are split into two halves in the horizontal direction.

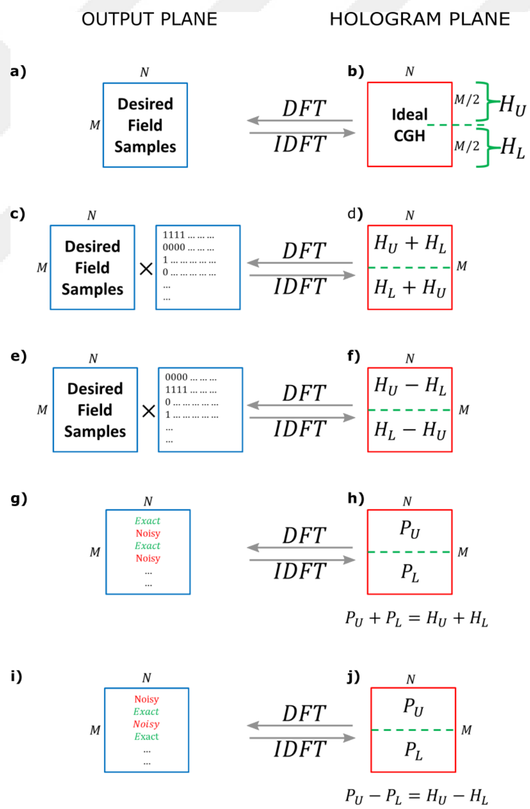

Figure 2.2. Basics of the proposed phase CGH computation method. All signals are discrete. a) Desired field S. b) Ideal full-complex CGH H with two halves named H_U and H_L. c) Downsampling of S. Only even rows (rows with even index such as $k = 0, 2, \ldots$) are preserved. d) Corresponding CGH, aliased as a result of downsampling. e) Downsampling of S. Only odd rows are preserved. f) Corresponding CGH. h) A phase CGH satisfying $P_U + P_L = H_U + H_L$ ($|H_U + H_L| \leq 2$), computed as in Fig. 2.1(b). g) The field generated by h. In accordance with c and d, h generates the same even rows with H. Odd rows however are left uncontrolled and appear noisy. i-j) Counterpart of g-h for perfect reconstruction of odd rows. Phase CGHs exactly control half of the degrees of freedom, as expected.

In summary, we have developed a method that computes a phase CGH that perfectly reconstructs half of S via a single FFT and trivial arithmetic operations. The simulations in Fig. 2.3 verify the method, and at the same time illustrate the first attempt for its usage in HIP. Figure 2.3(a) shows the magnitude of a desired S. The phase, not illustrated, is assigned randomly. Figure 2.3(b) shows the corresponding ideal CGH, H (magnitude). Figure 2.3(c) shows a phase CGH designed to reproduce the even rows (phase is shown as a gray scale image with black and white pixels denoting no and full 2π phase modulation, respectively). Figure 2.3(d) shows the generated S. As seen, even rows are perfectly reconstructed. Odd rows however, are left uncontrolled and appear noisy. Figure 2.3(e) and Fig. 2.3(f) show the dual case where odd rows are perfectly reconstructed and even rows appear noisy.

One disadvantage of the presented method, as evident in Fig. 2.3, is that the signal and noise samples are interlaced into each other. Thus, in the output, the encoding noise appears distributed and the reconstructed images appear highly noisy. It would have been better if the controlled half of the samples were grouped together within a signal window, and the uncontrolled half were grouped together within a noise window. However, to our knowledge, a direct non-iterative solution for that case is not possible. Fortunately, it is possible to further tailor the basic method such that the effect of the encoding noise is reduced. We explore that possibility in the next section.

An important requirement of the proposed method is that the illumination wave should have a uniform intensity over the SLM. The reason is, the entire method relies upon the assumption that unit magnitude pixels in the two halves (upper and lower, or left and right) of the phase-only SLM are superposed to form complex-valued pixels. If the actual illumination is not uniform, different complex pixel values are realized, and we get additional noise on the reconstructions. Of course, the entire illumination wave should have the necessary degree of spatial and temporal coherence so that the light from two halves of the SLM interfere.

We finally note that for sake of clarity, we explained our method for a 2-f setup. If it is desired to free the system of any lenses, one option is to perform reconstructions at the far field, where the Fraunhofer diffraction formula applies. For closer distances where the wave distributions on SLM and image planes are related by Fresnel diffraction formulas, the proposed method still works if phase CGHs are multiplied by QPF

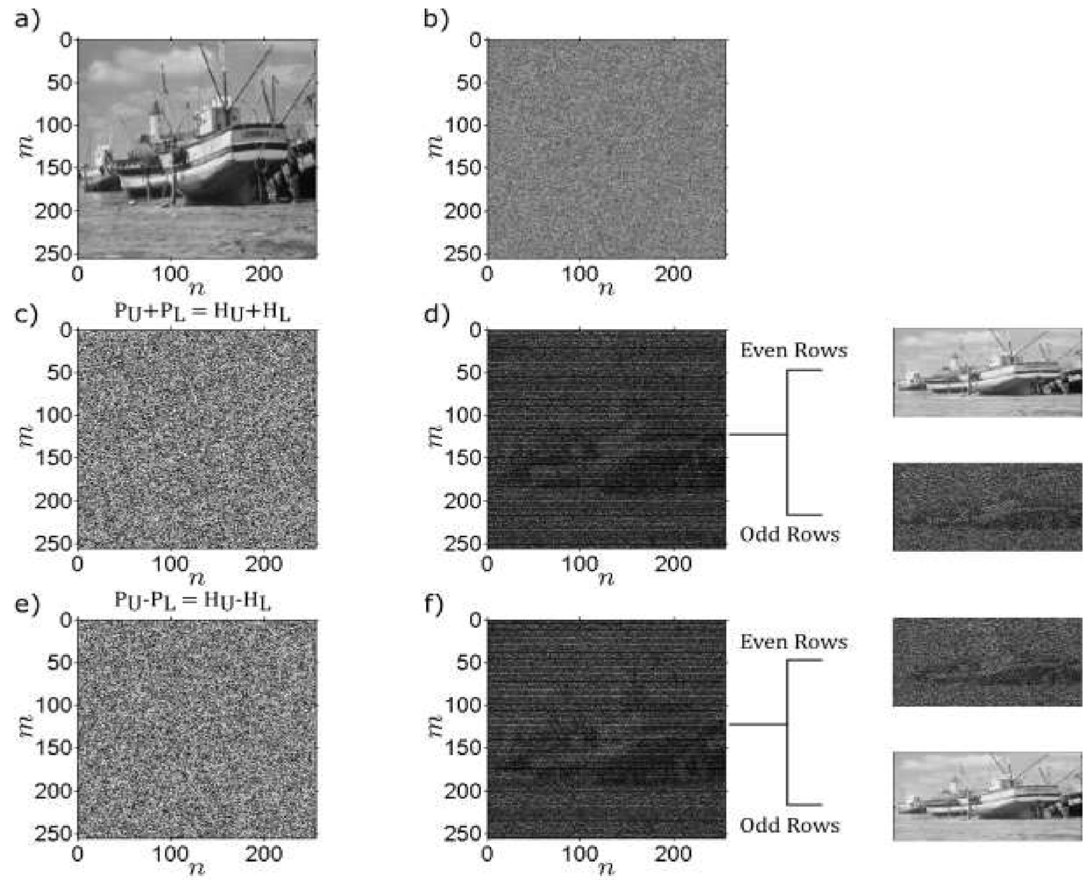

Figure 2.3. Verification of the basic phase CGH computation method. (a) Desired field S. Only magnitude is shown. Phase is random. (b) Magnitude of ideal full-complex CGH H. (c) Phase CGH satisfying $P_U + P_L = H_U + H_L$, shown as a gray scale image. (d) Reconstruction of c and its downsampled versions. (e) Counterpart of c-d for phase CGH satisfying $P_U - P_L = H_U - H_L$.

terms that undo the pre-multiplicative chirp term of Fresnel diffraction [57].

2.2 Application to holographic image projection

In HIP, we wish to set the intensity distribution on the Fourier plane of the phase-only SLM to that of a desired image. We examine two different cases that are illustrated in Fig. 2.4. In the first case, we target the entire CDO region (with area $\frac{\lambda f}{\Delta_x} \times \frac{\lambda f}{\Delta_y}$), i.e., the desired image extends over a full period. In the second case, we target only half-of the CDO (with area $\frac{\lambda f}{2\Delta_x} \times \frac{\lambda f}{\Delta_y}$ or vice versa) and confine the desired image here.

The other half is used as a don't care region and reserved for the encoding noise. The first case is advantageous in terms of light efficiency, while the second case enables the achievement of lower reconstruction error. In both cases, we eventually use the basic method described in Section 2.1. However, we apply initial phase distributions on the desired image prior to the application of the basic method in order to keep the encoding noise low. The initial phase distributions also provide speckle reduction. We also discuss strategies in which we calculate multiple phase CGHs for a given image, display them time sequentially, and make use of temporal averaging to further improve quality of the reconstruction.

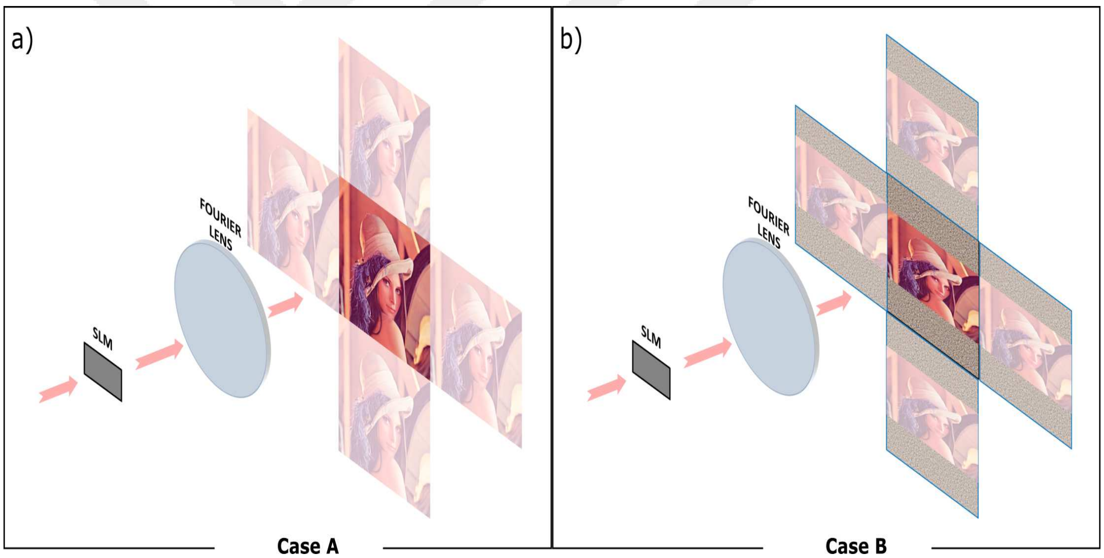

Figure 2.4. Examined HIP scenarios. (a) Desired image is specified over the entire central diffraction order (CDO). Phase freedom on the image plane is exploited to decrease encoding error. (b) Desired image is specified over half of the CDO. The unused part of CDO is reserved for encoding noise.

2.2.1 Case A: Image extends over the entire CDO

When the entire CDO is used as the image area, the only way to mitigate the CGH encoding noise is to make use of the phase-freedom on the image plane [17, 38, 53]. Phase terms applied on the target images are designed to create a more uniform energy distribution on the SLM plane. In that way, encoding noise is reduced. Similar to the case in Fig. 2.3, most algorithms apply a random phase distribution which leads to high speckle noise. Recently, Shimobaba et. al. proposed the application of a quadratic phase function (QPF) rather than a random phase term [58]. Their QPF term essentially maps the diffracted version of the target image in a 1-1 fashion on the SLM. As a result, energy extends over the entire SLM. Subsequently, they apply the Error Diffusion algorithm and get reconstructions with low encoding noise. The non-random nature of their QPF term also leads to reduced speckle noise. Our solution is similar, but with some difference in the applied QPF term. More importantly, in the second stage, rather than Error Diffusion, we apply the basic method presented in Section 2.1, which is much faster.

We first divide the target image into two parts that have almost the same energy as in Fig. 2.5(a). We map one of these parts to the upper half of the SLM via a suitably adjusted QPF term. The second part is mapped to the lower part of the SLM via another QPF term. In this way, we ensure that image energy is distributed pretty smoothly over the SLM area, which helps to keep the encoding noise low. The energy based splitting of the desired image, rather than a simpler splitting into two equally sized sub-images, is preferred here to handle cases where one-half of the image has significantly lower energy compared to the other. We also adjust the QPF terms such that some safety region is left at the boundary between the two halves of the SLM. In particular, the middle rows of the SLM do not carry significant information. In this way, we ensure that the harsh aperture windows that we apply when extracting H_U and H_L out of H do not cause significant diffraction artifacts. Finally, we apply the basic method in Section 2.1 on H and determine a phase CGH. Here, we do not shuffle $\vec{P}_1$ and $\vec{P}_2$ among P_U and P_L, but we orderly set all pixels of P_U to $\vec{P}_1$ and all pixels of P_L to $\vec{P}_2$ (or vice versa) as shown in Fig. 2.6(a). In this way, we ensure that the encoding noise on the odd rows has a low-pass nature and is better controlled. Figure 2.7(a) shows a desired image, and Fig. 2.7(b) shows the corresponding ideal full-complex CGH obtained as described above. Figure 2.7(d) shows the reconstruction performed by a phase CGH designed to perfectly reconstruct the even rows. Thanks to the applied initial phase term, the encoding noise distributed on the odd rows has reduced effect on the overall image. Speckle noise is also reduced.

The idea can be extended to phase CGHs for even or odd columns in a straight-forward manner. In that case, the desired image and the SLM is split into two parts horizontally, rather than vertically, and QPF terms are modified accordingly. Figure 2.7(c) shows the ideal full-complex CGH for the column case, and Fig. 2.7(e) shows the reconstruction when phase CGH is computed for even columns.

Careful examination of Fig. 2.7(d) and Fig. 2.7(e) reveal that although the effects of encoding and speckle noise are reduced, some ghost replica artifacts are present in the reconstructions. Such artifacts occur as a consequence of the mixing performed between the two halves of the SLM when computing the phase CGHs, and appear dominantly on the reconstruction when only a single phase CGH is used per a desired image. However, further improvements can be achieved by exploiting the finite temporal response time of the human visual system. In particular, for a given desired image, more than one CGH can be computed such that each CGH reconstructs one of even rows, odd rows, even columns and odd columns perfectly. Then these CGHs can be displayed time sequentially and temporally averaged. Figure 2.7(f)-2.7(h) show temporally averaged reconstructions for different combinations of two or four CGHs. As seen, the encoding noise is smoothed further, but at the cost of divided SLM frame rate.

The reader can truly claim that any CGH computation method (including the simplest direct quantization method) can have an improved error performance when temporal averaging is allowed, and may wonder what difference our method has in comparison. Actually, our method makes more efficient use of temporal averaging compared to other methods. To see this, consider a CGH computed for even rows. The image generated by this CGH has a high error partly due to the fact that the information on the odd rows is discarded [Fig. 2.7(d)]. That missing piece of information is restored if a second CGH is computed for odd rows, and used in conjunction with the first CGH in a time averaged fashion [Fig. 2.7(f)]. In other words, time averaging not only smooths out encoding noise, but also completes the information content. Therefore, the improvement in error is stronger. Temporal averaging of two row CGHs provide significant improvement over a single CGH, but actually a set of four CGHs that include the column CGHs as well is better. The reason is, the ghost replica artifacts for even and odd row CGHs appear at the same locations, and hence appear persistent even under temporal averaging. However, the ghosts of column CGHs appear at different positions [Fig. 2.7(g)]. So, if they are included in the time-averaging process, the effect of the artifact is reduced [Fig. 2.7(h)]. We also note that although we compute four CGHs, the computation requires only two FFT operations, one for row CGHs, one for column CGHs. Hence, computational efficiency of the algorithm is still preserved.

Table 1 reports the performance of the proposed algorithm under different temporal averaging schemes. For each case, the algorithm is applied on a test set including the well-known *Lena, Cameraman, Boat, Peppers, Mandrill* images, and the average mean-squared error (MSE) [27] and structured similarity index measure (SSIM) [59] values are reported, along with the required number of FFT operations per image (not per reconstruction) and the demanded SLM frame rate to deliver a monochrome video with a frame rate specified by **F**. Image quality improves as more reconstructions are averaged, with the 4-average case performing the best. Table 2 provides a comparison of our 4-average algorithm with the Iterative Fourier Transform Algorithm (IFTA), which is generally known to yield the best error performance. Each row of Table 2 specifies the number of reconstructions to be averaged per image and the number of IFTA iterations required for each reconstruction, such that the MSE performance of the 4-average case is achieved. The indicated iteration numbers are again averaged over the above-mentioned image set. Also note here that the third column of Table 2 is reported by taking into account that IFTA requires two FFTs per iteration. Tables 1 and 2 clearly highlight the high computational efficiency of our solution.

In closure, we note that the level of the ghost replica and ringing artifacts can be further reduced by performing a small number of IFTA iterations on the phase CGHs obtained with our method. In terms of computational complexity, this strategy slightly hinders the advantage of our non-iterative method, but is still better compared to IFTA solutions starting from random initial CGHs since our phase CGHs already have a low error, enabling faster convergence. Increasing the number of IFTA iterations used per phase CGH, the required number of temporal averages hence the SLM frame rate can be decreased as well. Thus, a trade-off between required SLM frame rate, reconstruction quality and computational complexity can be established. We also remind that the artifacts are a result of our speckle reduction goal (i.e. the artifacts only appear in Fig. 2.7 where we use structured initial phase terms, but do not appear in Fig. 2.3 where we use random phase terms). If some controlled amount of randomness is allowed on the initial phase terms applied on the images, the level of artifacts can be reduced at the expense of increased speckle noise as well.

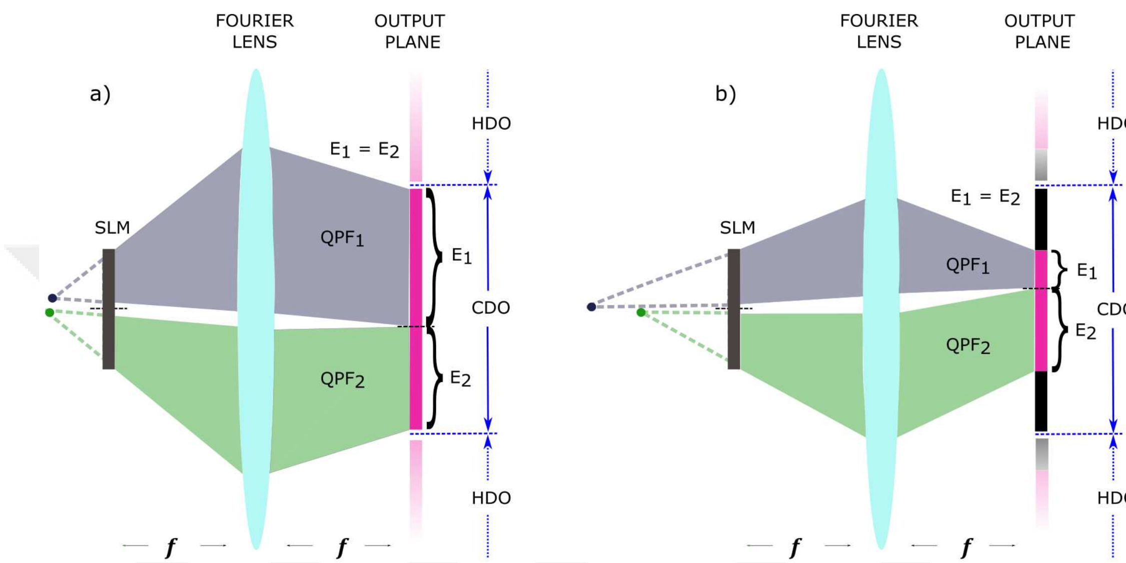

Figure 2.5. Initial phase terms (Quadratic Phase Functions - QPF) applied on the desired images to obtain a smooth energy distribution on the SLM plane. Desired image occupies (a) the entire CDO, (b) half of the CDO. In both cases, desired image is split into two parts with almost equal energies E_1 and E_2. In general, the two parts have different sizes. The upper (lower) part is mapped to upper (lower) half of the SLM via a suitable QPF term, which actually acts as a lens term that locally adjusts the ray directions for the mapping. In this way, image energy is distributed uniformly on the SLM, enabling a low encoding noise. The middle region of the SLM is left relatively empty to avoid diffraction artifacts during the calculation of phase CGHs.

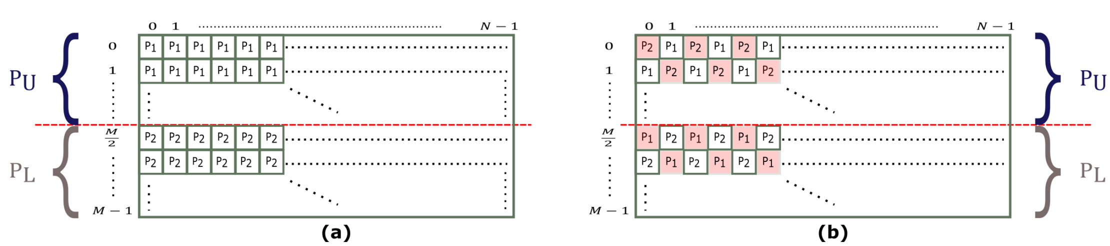

Figure 2.6. Assignment of $\vec{P}_1$ and $\vec{P}_2$ to P_U and P_L in (a) Case A (b) Case B, where pixels on a checkerboard pattern are flipped with respect to Case A.

Table 2.1. Performance of the proposed HIP algorithm for Case A. The average Mean Squared Error (MSE) and Structured Similarity Index Measure (SSIM) values of a set of desired images is reported.

Number of Reconstructions per Image	MSE (%) (average)	$SSIM$ (max : 1) (average)	Number of FFT per Image	Required SLM fps (**F** : video fps)
1	47.3	0.31	1	**F**
2	21.9	0.44	1	**F** $\times$ 2
4	12.3	0.52	2	**F** $\times$ 4

Table 2.2. IFTA configurations that achieve the MSE performance of the last row of Table 1.

Number of Reconstructions per Image	Number of Iterations per Reconstruction (average)	Number of FFT per Image (average)	Required SLM fps (**F** : video fps)
1	> 60	> 60	**F**
2	10.8	43.2	**F** $\times$ 2
3	3.4	20.4	**F** $\times$ 3
4	1.5	12	**F** $\times$ 4

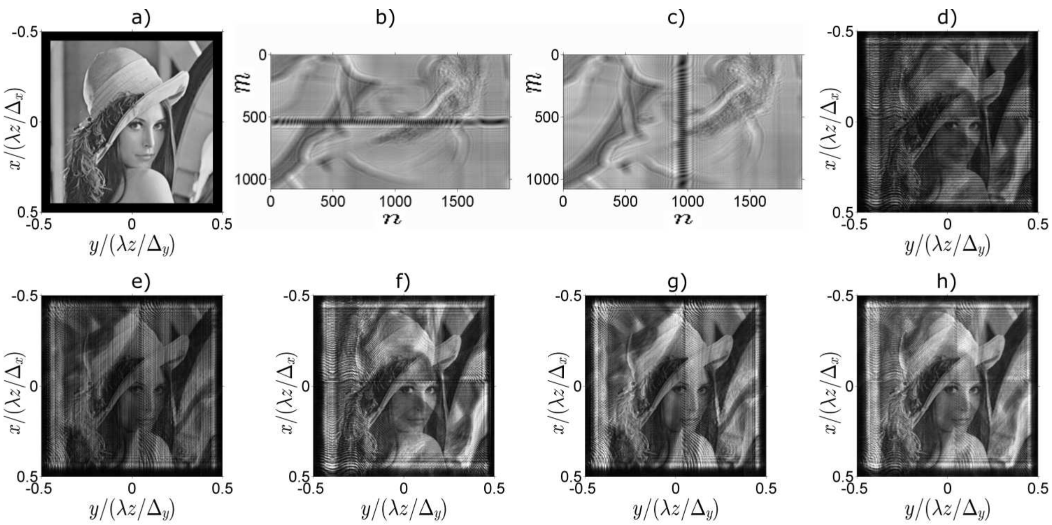

Figure 2.7. Simulation results for *Case A*. a) Desired image specified within the entire CDO. b,c) Ideal full-complex CGHs respectively for the row and column cases, obtained by the application of the QPF terms in Fig.2.5(a). d,e) Reconstructions by phase CGHs designed respectively for even rows and even columns. Reconstructions by phase CGHs for odd rows and columns look similar. f) Time averaged reconstruction by two phase CGHs designed for even and odd rows. g) Time averaged reconstruction by two phase CGHs designed for even and odd columns. In f and g, two SLM frames are required to form each video frame. h) The average of f and g, requiring 4 SLM frames per video frame. In d and e, there are missing pixels and artifacts, hence reconstruction error is high. Note also that the artifacts in d and e appear at different locations. In f and g, information is completed, but artifacts appear persistent since only reconstructions by row or column type CGHs are averaged. In h, information is complete and artifacts are relatively suppressed, hence best image quality is achieved.

2.2.2 Case B: Image occupies half of the CDO

When only half of the CDO is used for image projection, the unused half can be used to distribute the encoding noise. Therefore, compared to Case A, images with much lower error values can be expected. Phase CGHs for this case are mostly computed with the Fineup with Don't Care (FIDOC) or Direct Search algorithms, which are again iterative [16, 31, 42]. We now show that our non-iterative basic method can also be extended to this case. Figure 2.8(a) shows a desired image that occupies merely half of the CDO. We apply two QPF terms to this image and distribute it on the SLM area as in the previous case [Fig. 2.5(b)]. The QPF terms are designed for the column case, and are adjusted to handle the smaller image area. Figure 2.8(b) shows the resulting

H. Next, we compute the phase CGH for even columns. At this stage however, we make the following change relative to Case A: if $m + n$ is even, we flip $\vec{P}_1$ and $\vec{P}_2$, as shown in Fig. 2.6(b). If $m + n$ is odd, we make no changes. This modification is inconsequential when sum of pixels is considered. Therefore, even columns are still reproduced exactly. However, difference of pixels is changed, thus the odd columns generated by the CGH are changed. The high-frequency modulation we impose shifts the encoding noise from the image area to the unused portions of the CDO, as evident in the reconstruction provided in Fig. 2.8(c). The image area receives quite minor contribution from encoding noise. The reconstructed image appears fine, but has high error due to the fact that odd rows are missing ($MSE = 33\%$, $SSIM = 0.69$). To complete the image, we compute a second CGH for odd columns. When the two CGHs are displayed time sequentially, we obtain the time-averaged image shown in Fig. 2.8(e). The image has a high quality and a quite low error ($MSE = 3\%$, $SSIM = 0.76$). On the contrary to the previous case, four CGHs are not needed in time averaging, but two CGHs suffice, since ghost replica artifacts appear in the unused areas of CDO.

To provide a comparison, we applied our time-averaged solution (two SLM frames and 1 FFT for each image) and the FIDOC algorithm (1 SLM frame per image, 2 FFT per iteration) on the image set used in Case A. The average MSE error with our solution is 2.9%, while the same MSE performance requires on the average 10.6 iterations (corresponding to 21.2 FFTs per image) with the FIDOC algorithm. When two FIDOC reconstructions are temporally averaged, we require on the average 5.2 iterations to be performed per reconstruction to match the MSE value of our proposed method (yielding a similar demand of $2 \times 2 \times 5.2 = 20.8$ FFTs per image).

2.3 Experimental results

We carried out proof of concept HIP experiments with the setup illustrated in Fig. 2.9(a) to verify our CGH computation algorithm. The light source is a He-Ne laser and the computed phase CGHs are displayed on a Holoeye-Pluto SLM having $8\ \mu m$ pixel pitch and 8-bit modulation depth. The modulated light beam coming out of the SLM is directly projected onto the CCD array of a camera without any spatial filtering. The camera is placed slightly off-axis to avoid the unmodulated (i.e. direct, DC) beam of the SLM. A linear phase term is superimposed on the phase CGHs to perform off-axis reconstructions.

Figure 2.9(b) shows the experimental result for Case A of Section 2.2 where the desired image occupies the entire CDO. The image is obtained as the average of the reconstructions of four phase CGHs computed for even/odd rows/columns. Figure 2.9(c) shows the result for Case B of Section 2.2 where the desired image is limited to half of the CDO. This time, we show the average of the reconstructions of only two CGHs. Although the experimental results verify the presented algorithm, there is some discrepancy and loss in image quality in comparison to the simulation results in Fig. 2.7 and Fig. 2.8, which is attributed to the non-idealities of the SLM, such as pixel cross-talk and flickering of liquid crystal cells.

To provide a comparison of image quality, Fig. 2.9(d) shows the counterpart of Fig. 2.9(b) obtained with IFTA algorithm (average of 4 reconstructions, 2 iterations per reconstruction). It is clearly seen that our method significantly reduces the speckle noise, however, at the cost of some ghost replica or ringing artifacts. A counterpart of Fig. 2.9(c) with FIDOC algorithm is not provided, since the image appearance is almost the same, although with our algorithm computation is much faster.

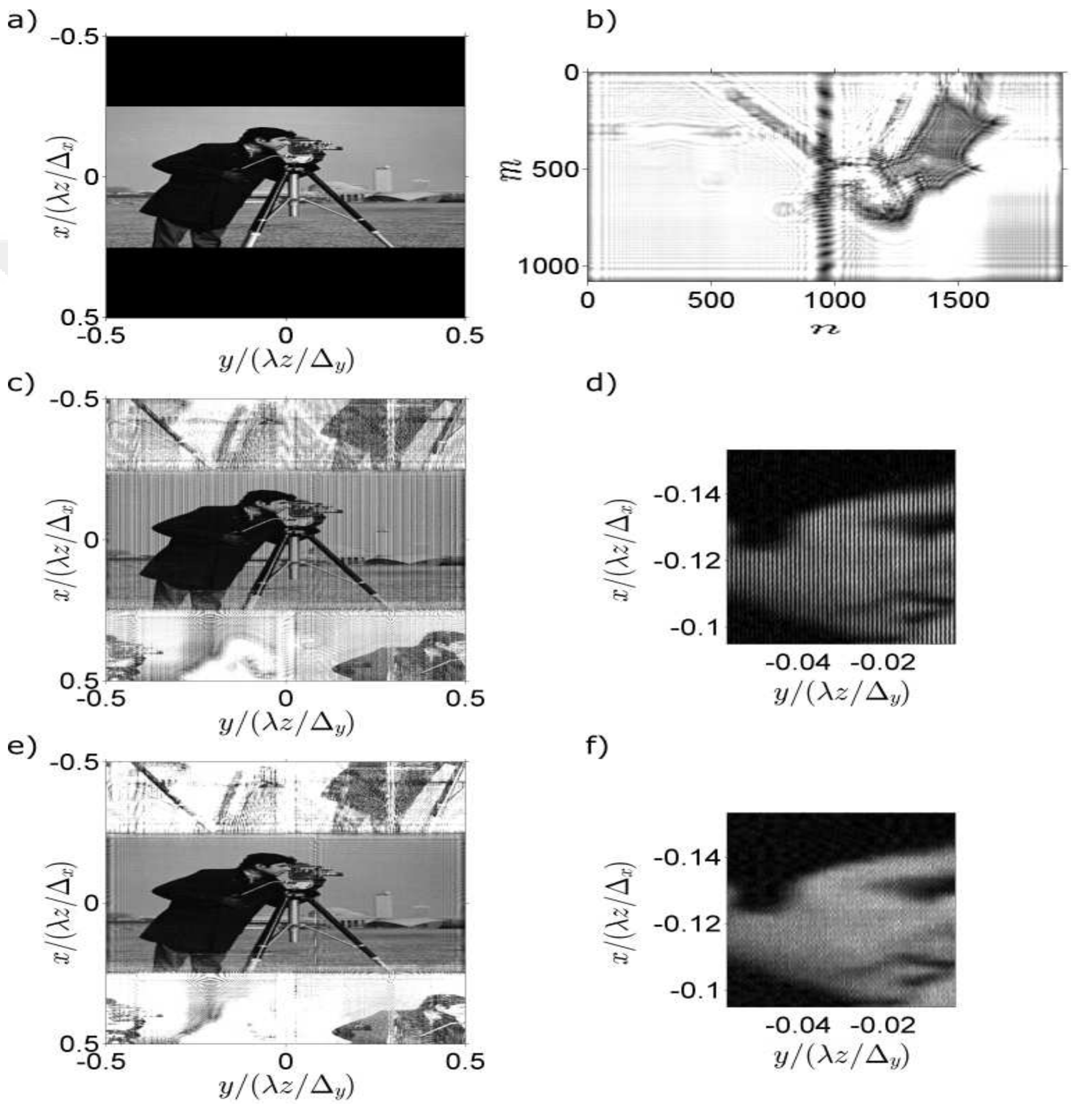

Figure 2.8. Simulation results of *Case B*. (a) Desired image within the CDO. Dark regions are reserved for encoding noise. (b) Corresponding ideal full-complex CGH, obtained by the application of the QPF terms in Fig.2.5(b). (c) Reconstruction by a phase CGH designed for even columns. Encoding noise mainly appears in the unused part of CDO, and odd columns within the image area appear as missing, rather than noisy, similar to that in interlaced video format. (d) Zoom-in version of c. (e) Average of the reconstructions of two phase CGHs for even and odd columns. (f) Zoom-in version of (e). In e and f, full information is restored, and speckle and encoding noise is quite low.

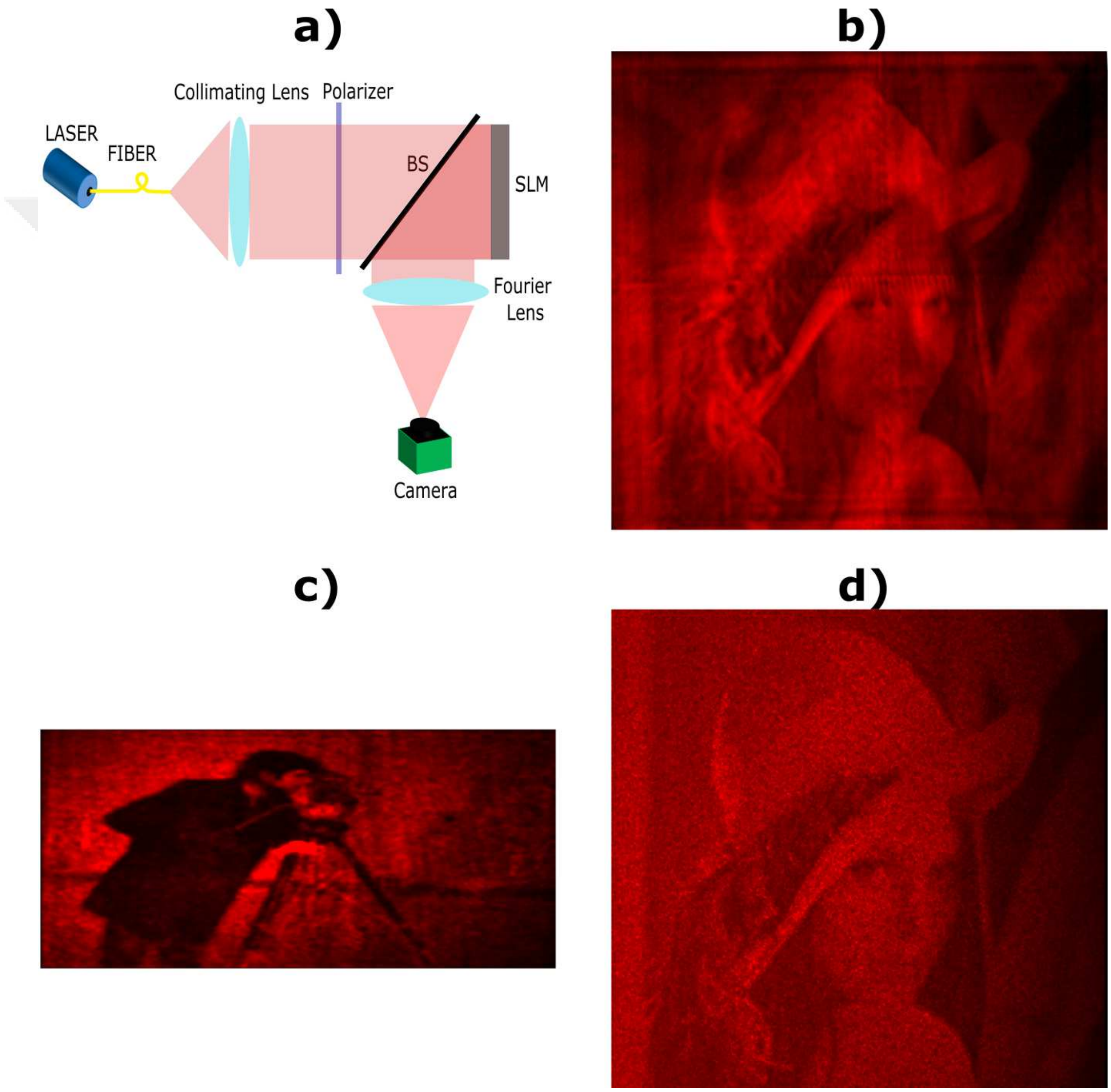

Figure 2.9. a) Experimental HIP setup. Camera is placed slightly off-axis to avoid the unmodulated beam of the SLM. b) HIP Case A, average of reconstructions of four phase CGHs. Experimental version of Fig. 2.7(f). c) HIP Case B, average of reconstructions of two phase CGHs. Experimental version of Fig. 2.8(e). The lower quality in comparison to simulation results is due to SLM pixel cross-talk and flicker effects. d) HIP Case A obtained with IFTA algorithm, which makes the speckle reduction ability of our algorithm quite evident.

3 HIGH QUALITY SPECKLE FREE PHASE ONLY COMPUTER GENERATED HOLOGRAPHIC IMAGE PROJECTION

In this chapter, we present a new phase CGH computation algorithm, in which we (1) design an initial image specific phase term, (2) impose that on the target image and compute an initial CGH, (3) use the initial CGH as the starting point of iterations. The merit of the algorithm over the previously discussed cases is that, the initial CGH computed in step 2 is already very close to a phase-only function (thanks to the image specific initial phase term in step 1), therefore, the iterations in step 3 converge quickly to unprecedently low-error phase CGHs whose reconstructions are almost speckle-free. The method also works for full FOV (i.e. does not require a partioning of available image area among signal and noise windows) and thus provides maximum light efficiency.

3.1 Phase freedom on image plane in HIP

We begin our discussion by stating that mostly formulations of the phase CGH computation problem assume that the image is reconstructed at a Fourier plane of the SLM as shown in Figs. 2.1(a) and 3.1 [16, 16, 17, 18, 31, 38, 44]. The devised methods are extended in a straightforward manner for more general cases where image and SLM planes are related by Fresnel or fractional Fourier Transforms since these are essentially Fourier Transforms with pre and post multiplications with pure phase functions [5, 37, 57, 60]. In the Fourier plane formulation, if $I(x, y)$ denotes the intensity of a target image, the goal is to find a CGH $h(u, v)$ such that $|h(u, v)|^2$ is constant and $|H(x, y)|^2$ equals $I(x, y)$ as much as possible, where $H(x, y) = \mathcal{F}\{h(u, v)\}$. A first option is to calculate an initial CGH as $h(u, v) = \mathcal{F}^{-1}\{\sqrt{I(x, y)}e^{j0}\}$ (i.e., zero phase on the image) and then discard the magnitude information to obtain a pure phase CGH. This simple option performs poorly though, since $h(u, v)$ calculated as above usually exhibits a strong central peak due to the fact that typical images have a low-pass nature, as conceptually illustrated in Fig. 3.1(a). Here image and SLM planes are located at the focal planes of a 2-f setup, and a staircase function represents the low-pass target image. The initial CGH can be considered to be obtained by illuminating the image from left to right with a normally incident plane wave (parallel rays) and backtracing these rays to the SLM plane. The low-pass nature of $\sqrt{I(x, y)}e^{j0}$ creates almost negligible diffraction spread, so all the rays leaving the image plane essentially remain at normal incidence and get focused at the right focal point of the Fourier lens, leading to a CGH with the strong central peak discussed above. Such a CGH leads to a large error in the form of a strong high-pass filter effect (since high frequency information is boosted relative to low-frequency information) when the magnitude information is discarded, as verified by the one dimensional simulation shown on Fig. 3.2(a) for a more complicated target image.

A better option, and the most common approach, is to obtain an initial CGH as $h(u, v) = \mathcal{F}^{-1}\{\sqrt{I(x, y)}e^{j\phi(x,y)}\}$ where $\phi(x, y)$ is a random function. This approach optically corresponds to the placement of a random diffuser on the image plane that shuffles the ray directions, and creates a CGH with a more uniform energy distribution, as illustrated in Fig. 3.1(b). This technique, upon direct quantization, leads to a smaller error and a better reconstruction. However, the introduction of the random diffuser causes significant speckle noise, as verified in Fig. 3.2(b). Usually, further iterations are carried out back and forth between SLM and image planes to improve image quality, as in Gerchberg-Saxton or iterative Fourier transform (IFTA) type algorithms [34, 36, 38, 39]. However, in such solutions, convergence is rather slow and speckle effects persist to a non-negligible extent at the final image. Fine-up with don't care (FIDOC) algorithms reduce speckle noise and facilitate convergence considerably but only at the cost of reduced field of view (FOV) and decreased light efficiency by sparing part of the available image area to distribute quantization noise [16, 31, 42].

A third approach is to obtain an initial CGH as $h(u, v) = \mathcal{F}^{-1}\{\sqrt{I(x, y)}e^{j\pi\alpha(x^2+y^2)}\}$ (i.e., impose a quadratic phase function (QPF) on the image) [61, 62]. By suitably adjusting the α parameter of the QPF, the image can bit fitted in the SLM aperture in a 1-1 mapping fashion. Optically, this approach corresponds to the placement of a thin lens at the image plane, as illustrated in Fig. 3.1(c). The focal length of the lens is controlled by α. Similar to the random phase case, the initial CGH has a better distribution of energy. Moreover, the non-random nature of the applied phase term (the ordered mapping between image and SLM points) leads to significant speckle reduction. However, direct quantization leads again to poor results since the energy distribution is not uniform, due to the fact that the image intensity is not necessarily uniform, as verified in Fig. 3.2(c). Subsequent algorithms such as Error Diffusion (ED) improve reconstructions again only when image size and light efficiency are reduced [43, 58].

The basic idea behind our algorithm is illustrated in Fig. 3.1(d). We first divide the target image into a number of blocks (four in this case, one for each stair of the image). Then, for each block, we design a separate phase function, consisting of prisms and lenses with custom tilt angles and focal lengths. The prisms and lenses are designed such that each block is mapped on an SLM region with an area proportional to its energy content. For instance, the purple block, having the highest energy content, is mapped to the largest SLM area, while the red block, having the smallest energy content, is mapped to the smallest SLM area. In this way, we ensure that the energy distribution on the SLM plane is almost uniform. Therefore, the resulting CGH is almost readily phase-only, leading to quite small error even when directly quantized, as verified by the simulation in Fig. 3.2(d). The fact that the image plane in Fig. 3.1(d) is mapped in an orderly manner on the SLM plane (rather than in a random manner) also ensures that speckle noise is kept minimal. In Section 3.2, we provide the mathematical background of the proposed method for the case of one-dimensional signals. In Section 3.3, we discuss the extension of the method for two-dimensional signals. Section 3.4 and 3.5 present simulation and experimental results, respectively.

3.2 Basic Method - One dimensional signals

In this section, we discuss the mathematical background of our method in the one-dimensional (1D) signal domain. Our assumptions are as follows: as in Fig.1, the SLM and the image planes are located at the two focal planes of a lens. The complex transmittance of the SLM and the wavefield on the image plane are denoted by $h(u)$ and $H(x)$, respectively. The SLM is illuminated by a normally incident plane wave

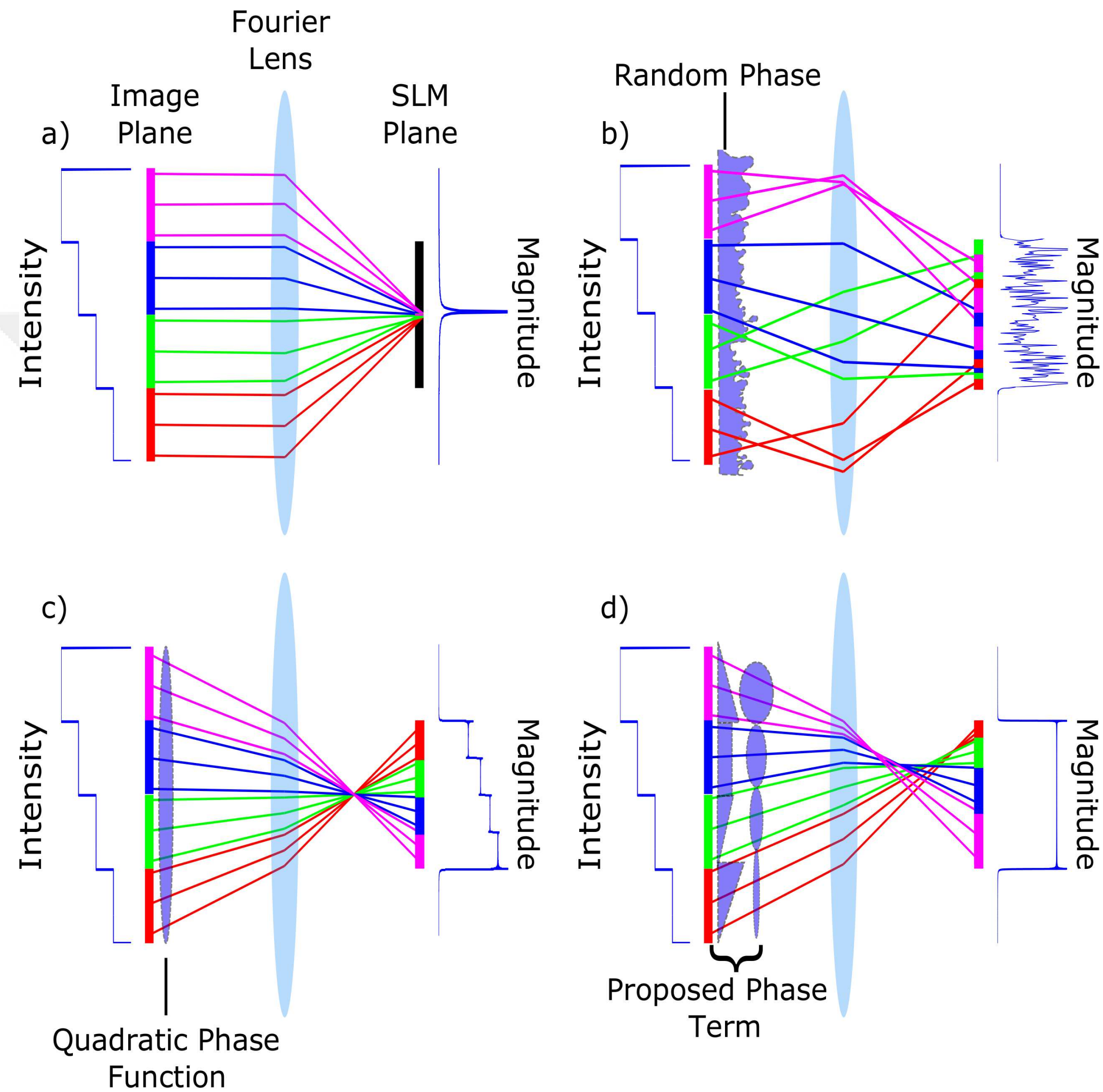

Figure 3.1. The effect of the initial phase function imposed on a typical low-pass target image prior to the computation of a phase CGH. a) No (constant) phase results in a CGH with a strong concentration of energy that leads to a large error when magnitude information is discarded (i.e. direct quantization) to obtain a phase CGH. b) A random phase (optically equivalent to a random diffuser) leads to a CGH with a better distribution of energy and thus lower error. The shuffled nature though results in high speckle noise. c) A quadratic phase function (QPF, optically equivalent to a lens) leads to a CGH with an ordered but not necessarily uniform distibution of energy. Thus, speckle noise is suppressed, but there is still non-negligible error. d) Proposed phase term (optically equivalent to block specific lenses and prisms) that results in a CGH with an almost uniform and ordered distribution of energy (i.e. a CGH that is readily phase-only) leading to speckle-free high quality reconstructions.

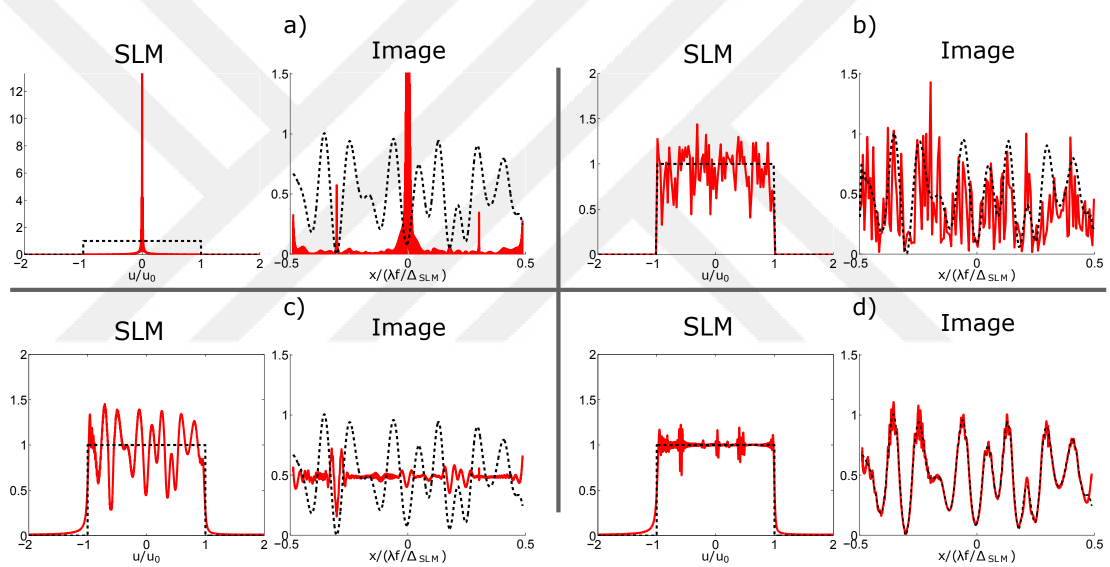

Figure 3.2. One-dimensional simulations that verify the four cases illustrated in Fig. 3.1. a) No (constant) phase function is imposed on the target image. The magnitude of the resulting wavefield on the SLM plane is shown on the left (red curve). The dashed black rectangle indicates the SLM aperture. The reconstruction performed by the phase CGH (obtained by direct quantization) is shown on the right (red curve). The dashed black curve shows the ideal target image. b,c,d) The simulations when the phase functions applied on the target image are random, QPF and the proposed phase term, respectively.

of wavelength λ. The Fourier lens has a focal length f, where for simplicity we take $\lambda f = 1$ (other cases are handled trivially with a coordinate normalization). Thus, we get the simple FT and IFT relations

$$H(x) = \int_{-\infty}^{\infty} h(u) e^{-j2\pi ux} du, \tag{3.1}$$

$$h(u) = \int_{-\infty}^{\infty} H(x) e^{j2\pi xu} dx. \tag{3.2}$$

The SLM is assumed to have a finite size and a finite bandwidth so that $h(u) = 0$ outside the $u \in (-u_0, u_0)$ interval, and the uniquely addressable image area is limited to the $x \in (-x_0, x_0)$ interval. In the case of a phase-only SLM, $|h(u)|^2 = c$ where c is a real positive constant for $u \in (-u_0, u_0)$, and we wish to have $|H(x)|^2 = I(x)$ for $x \in (-x_0, x_0)$, where $I(x)$ denotes the intensity of the target image. As explained in Section 1, our method comprises the design of an image specific phase term $\phi(x)$ such that the image plane wavefield $H(x) = \sqrt{I(x)} e^{j\phi(x)}$ almost readily corresponds to an SLM plane wavefield $h(u)$ where $|h(u)|^2$ is as constant as possible within the SLM aperture.

We start by elaborating on the mechanism by which $\phi(x)$ influences the energy distribution of $h(u)$. For a smoothly varying $\phi(x)$, the function $H(x) = \sqrt{I(x)} e^{j\phi(x)}$ can be interpreted as an amplitude modulation (AM) signal, where $\sqrt{I(x)}$ represents the envelope and $e^{j\phi(x)}$ represents the carrier signal with a space-dependent modulation frequency. When $I(x)$ (and thus $\sqrt{I(x)}$) has a sufficiently narrow bandwidth (which is the case for typical images encountered in projection applications, as stated in Section 1), the frequency content of $H(x)$ is mainly determined by $e^{j\phi(x)}$ (as an example, consider the extreme case of $I(x) = 1$). In particular, suppose at some point $x_p \in (-x_0, x_0)$, the instantaneous frequency of $e^{j\phi(x)}$, defined as

$$u_{IF}(x) = \frac{1}{2\pi} \frac{d}{dx} \phi(x) \tag{3.3}$$

is equal to $u_p = u_{IF}(x_p)$. Then, the part of the image plane around x_p is essentially mapped around u_p on the SLM plane. Thus, $\phi(x)$ actually performs a mapping between image plane and SLM plane coordinates. This mapping is 1-1 if $\phi(x)$ is designed such that $u_{IF}(x)$ is monotonically increasing. From an optics perspective, $\phi(x)$ determines the local ray angle distribution on the image plane, as illustrated in Fig.1. The next question is, which mapping distributes the energy of the image as uniformly as possible on the SLM plane.

To answer the question above, we invoke a quantum optics perspective where the spatial coordinates U and X are interpreted as random variables (RVs) and $|h(u)|^2$ and $|H(x)|^2$ are interpreted as the associated probability density functions (PDFs) denoting the likelihood of detecting a photon at a particular spatial position (following appropriate amplitude normalizations, of course, that we skip now for simplicity). The fact that $|h(u)|^2 = c$ implies that U is a uniform RV. In this respect, what we want from the designed phase term $\phi(x)$ is to map the RV X characterized by the PDF $|H(x)|^2 = I(x)$ to a uniform RV.

A well-known theorem [63] from probability theory states that if U denotes a RV distributed uniformly in $(0, 1)$, and if X is another RV with a PDF given by $p_X(x)$, then X can be generated from U by the mapping:

$$Z = C_X^{-1}(U) \tag{3.4}$$

where $C_X(x) = \int p_X(x)dx$ denotes the cumulative distribution function (CDF) of X. Conversely, U can be generated from X by the mapping

$$U = C_X(X). \tag{3.5}$$

In summary, (1) $\phi(x)$ establishes a mapping between image and SLM plane coordinates, (2) $|h(u)|^2$ and $|H(x)|^2$ can be viewed as PDFs, and (3) a RV X is mapped to a uniform RV if it is input to its CDF function as $C_X(X)$. Combining these three pieces, we see that if we design a $\phi(x)$ such that $u_{IF}(x)$ as given in Eq. (3.3), after appropriate normalizations, is equal to $\int I(x)dx$ (the CDF function), then we get a CGH with a magnitude almost uniformly distributed over the SLM aperture. More precisely, let

$$C_I(x) = \frac{\int_{-x_0}^{x} I(x')dx'}{\int_{-x_0}^{x_0} I(x')dx'} \tag{3.6}$$

for $x \in [-x_0, x_0]$. Thus, $C_I(x)$ denotes the CDF corresponding to the target image, with $C_I(-x_0) = 0$ and $C_I(x_0) = 1$, as expected. Next, suppose we design an image specific phase function given as

$$\phi(x) = 2\pi u_0 \left(2 \int_{-x_0}^{x} C_I(x')dx' - x \right) \tag{3.7}$$

for $x \in [-x_0, x_0]$. Then, by Eq.3.3, the instantaneous frequency becomes

$$u_{IF}(x) = u_0 \left(2C_I(x) - 1 \right). \tag{3.8}$$

For $x \in [-x_0, x_0]$, we have $u_{IF}(x) \in [-u_0, u_0]$ with $u_{IF}(-x_0) = -u_0$, $u_{IF}(x_0) = u_0$. Also, $u_{IF}(x_2) \geq u_{IF}(x_1)$ for $x_2 \geq x_1$, i.e., $u_{IF}(x)$ is monotonically increasing. Thus $\phi(x)$ actually maps the target image on the SLM aperture in a 1-1, onto fashion. Moreover, the image energy is distributed almost uniformly on the SLM plane, since the mapping is equivalent to that in Eq. (3.5).

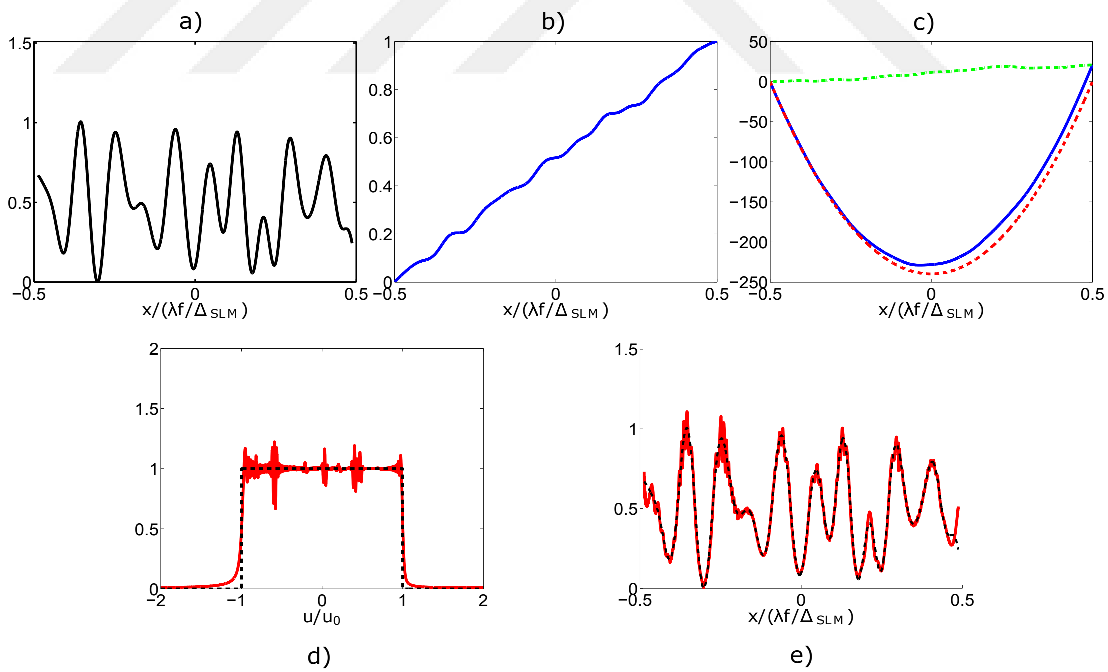

Figure 3.3. The application of the proposed method in the 1D signal domain. a) Intensity of the target image. b) The associated cumulative distribution function (CDF) as computed in Eq. (3.6). c) The phase function $\phi(x)$ computed as in Eq. (3.7) (blue curve) and imposed on the target image. The red curve shows a QPF to serve as a reference, with the green curve showing the difference. d) Magnitude of the resulting wavefield on the SLM plane, that is almost uniform in the SLM aperture. e) The intensity reconstructed by the phase CGH obtained by direct quantization.

Fig. 3.3 illustrates and verifies the described procedure. Fig. 3.3(a) shows an exemplary, one-dimensional target image $I(x)$ that is sufficiently low-pass. Fig. 3.3(b) shows the associated CDF, $C_I(x)$, found as in Eq.(3.6). The designed phase function $\phi(x)$, computed as in eq. (3.7), is shown by the blue curve in Fig. 3.3(c). To provide a comparison, on the same figure we include the QPF (the red parabola) which corresponds to the case $I(x) = 1$. The green curve shows the difference between the two curves. This figure emphasizes that ordinarily the designed phase functions deviate little from a QPF, but that little deviation has profound effects. In Fig. 3.3(d), the magnitude of the SLM field, $h(u)$, computed as in Eq.(3.2) is shown (red curve). As expected, $h(u)$ is almost readily a phase-only function that also fits in the SLM aperture (indicated by dashed black curve). The mere deviations from uniform magnitude behavior are in the form of ripples caused by rapidly falling or rising parts of the target image (i.e., those parts that slightly have a high frequency content). Finally, Fig. 3.3(e) illustrates the reconstructed intensity $|H(x)|^2$ (red curve) along with the desired one (black curve) when $h(u)$ in Fig. 3.3(d) is directly quantized into a phase-pattern by setting the magnitude to unity within the SLM aperture and to zero outside. As seen, a quite successful reconstruction that is also quite free of speckle noise is performed, verifying our case.

In Fig. 3.1, we conceptually explain our idea using image blocks and block-specific lenses and prisms. In this section though, we carry the discussion using PDFs and CDFs. The two views are in fact equivalent. In particular, in Fig. 3.1, if we increase the number of blocks so that block size approaches zero, the phase term corresponding to the lenses and prisms approaches that in Eq.(3.7). Therefore, the block based view is an approximation to the formulation presented here. In the one-dimensional case, the block based view can be totally discarded and we can use Eq.(3.7). In the two dimensional case though, the block based view gains practical importance, as will be explained in Section 3.3.

3.3 Two-dimensional signals

In this section, we extend our method developed in Section 1 to the case of two-dimensional signals. Unfortunately, due to several technical reasons that are discussed below, that extension is not straightforward. In particular, in general it is not possible to develop a 2D counterpart of the closed form expression in Eq.(3.7). However, it is possible to extend the block based view depicted in Fig.1d to the 2D case. In our development, we again follow the steps of Section 1, i.e., (1) the phase term designed and imposed on the image establishes a mapping between image and SLM plane coordinates through instantaneous frequencies, (2) image and SLM plane intensities are interpreted as PDFs, (3) the mapping is designed to map the arbitrary image plane PDF to the uniform SLM plane PDF. In this way, we distribute the energy on the image plane as uniformly as possible (so that phase quantization error becomes small) and in an ordered manner (so that speckle noise is avoided as much as possible) on the SLM plane.

With the inclusion of the second spatial dimension, the designed phase term $\phi(x, y)$ is now characterized by two instantaneous frequencies, one for each spatial dimension, as:

$$u_{IF}(x,y) = \frac{1}{2\pi}\frac{\partial}{\partial x}\phi(x,y) \ , \ v_{IF}(x,y) = \frac{1}{2\pi}\frac{\partial}{\partial y}\phi(x,y). \tag{3.9}$$

These frequencies now determine mappings between image coordinates (x, y) and SLM coordinates (u, v).

The second difference from the 1D case arises in the fact that $|h(u, v)|^2$ and $|H(x, y)|^2 = I(x, y)$ should now be interpreted as joint PDFs rather than marginal PDFs. In this respect, $\phi(x, y)$ should map the jointly distributed RV pair (X, Y) (characterized by $I(x, y)$) to the jointly distributed RV pair (U, V). By $|h(u, v)|^2 = c$, U and V are independent RVs, each having a uniform distribution. However, in general, X and Y are not independent unless $I(x, y)$ is separable as $I(x, y) = I_X(x)I_Y(y)$, which is the only case the 1D formulation in Section 3.2 can be applied independently along the two dimensions.

For a general joint PDF, the mapping of the RV pair (X, Y) to (U, V) can be accomplished in several ways. One alternative is the following mapping [63]:

$$U = C_{X|Y}(X, Y) \ , \ V = C_Y(Y) \tag{3.10}$$

where $C_Y(y)$ denotes the marginal CDF of Y, and $C_{X|Y}(X, Y)$ denotes the conditional CDF of X given Y.

Following the development of Section 2, we would be done if we could determine a $\phi(x, y)$ such that

$$u_{IF}(x, y) = u_0(2C_{X|Y}(y, y) - 1) \tag{3.11}$$

and

$$v_{IF}(x, y) = v_0(2C_Y(y) - 1). \tag{3.12}$$

However, we run into a problem here. In particular, suppose we try to find an analytical function $\phi(x, y)$ that satisfies Eq. 3.11 and Eq. 3.12 at all (x, y).. It is well-known that for an analytical function the mixed partial derivatives should be equal to each other, i.e., $\partial^2\phi/\partial x\partial y = \partial^2\phi/\partial y\partial x$. Though, in general that property is not satisfied by the $u_{IF}(x, y)$ and $v_{IF}(x, y)$ above. In other words, it is in general not possible to find a 2D counterpart for Eq. (3.7).

Having made this observation, we continue the extension of our method to 2D signals with the block based view that provides an approximate solution. This view, for the 2D case, is illustrated in Fig. 3.4(a). As seen, we divide the image plane into a number of rectangular blocks. Then, similar to that in Fig. 3.1(d), we design an off-axis lens term for each of the blocks, as shown in the inset. With these lenses, each block is essentially mapped on a particular patch on the SLM plane. Fig. 3.4(b) illustrates this mapping for some selected blocks on the image plane. Note that the patches in general have a quadrilateral shape. Patches for different blocks do not overlap, and the patches altogether cover the entire SLM area. In addition, the area of each patch is proportional to the energy content of the corresponding block. As a result, the target image is mapped on the SLM aperture in a geometrically distorted form such that the image energy is distribution on the SLM plane as uniformly as possible. This fact is illustrated in Fig. 3.4(c) and Fig. 3.4(d). Fig. 3.4(c) shows the *Cameraman* as the target image, while Fig. 3.4(d) shows the magnitude of the SLM field. Notice that though the black coat of the cameraman (corresponding to a low energy portion) covers a large area on the image plane, it is squeezed significantly on the SLM plane.

In the block based processing, we first insert the vertex coordinates of blocks into Eq. (3.11) and Eq. (3.12) and determine the corresponding vertex locations on the SLM plane, as in Fig. 3.4(b). Then, on the k^{th} block, we fit a phase fuction of the form

$$\phi^k(x,y) = \sum_{m=0}^{2}\sum_{n=0}^{2} \alpha_{m,n}^k x^m y^n, \tag{3.13}$$

which in general represents an off-axis, astigmatic, aberrated lens. Note that for this lens term, there are altogether 9 coefficients $\alpha_{m,n}^k$, and the instantaneous frequencies in Eq. (3.11) and Eq. (3.12) become $\frac{1}{2\pi}\sum_{m=1}^{2}\sum_{n=0}^{2} m\alpha_{m,n}^k x^{m-1}y^n$ and $\frac{1}{2\pi}\sum_{m=0}^{2}\sum_{n=1}^{2} n\alpha_{m,n}^k x^m y^{n-1}$, respectively. To determine $\alpha_{m,n}^k$, we write two equations for each vertex of the image block (one for each instantaneous frequency). In this manner, we altogether get 8 equations from which we determine 8 of $\alpha_{m,n}^k$ except for $\alpha_{0,0}^k$. Here, in general the equation set may not have a solution (due to the fact that mixed derivatives are not equal), thus we solve the equations in the minimum-least squared sense. The undetermined $\alpha_{0,0}^k$ is adjusted to ensure that the overall phase function is continuous and does not lead to diffraction artifacts in the final reconstruction. We finally obtain a CGH by performing an IFT on the target image superimposed by the designed phase function.

We close this section by noting that since $\phi(x,y)$ designed as described above performs the mapping in Eq. (3.10) only approximately, the reconstructions obtained by direct quantization of the computed CGHs are not as successful as their one dimensional counterparts. However, when a sufficiently large number of blocks are used, the calculated CGH serves as a quite nice initial point for iterative algorithms, enabling the achievement of quite minor error values with significantly facilitated convergence, as verified by the simulations presented in the next section.

3.4 Simulation Results

In this section, we present 2D simulations that verify the merits of our method. As for the metrics for assessing the quality of reconstructions, we use minimum-mean squared error (MSE), structured similarity index measure (SSIM), peak signal to noise ratio (pSNR) and speckle contrast (SC) [59, 64].

Fig. 3.5 shows a simulation where the target image is *Lena*. Fig. 3.5(a) shows

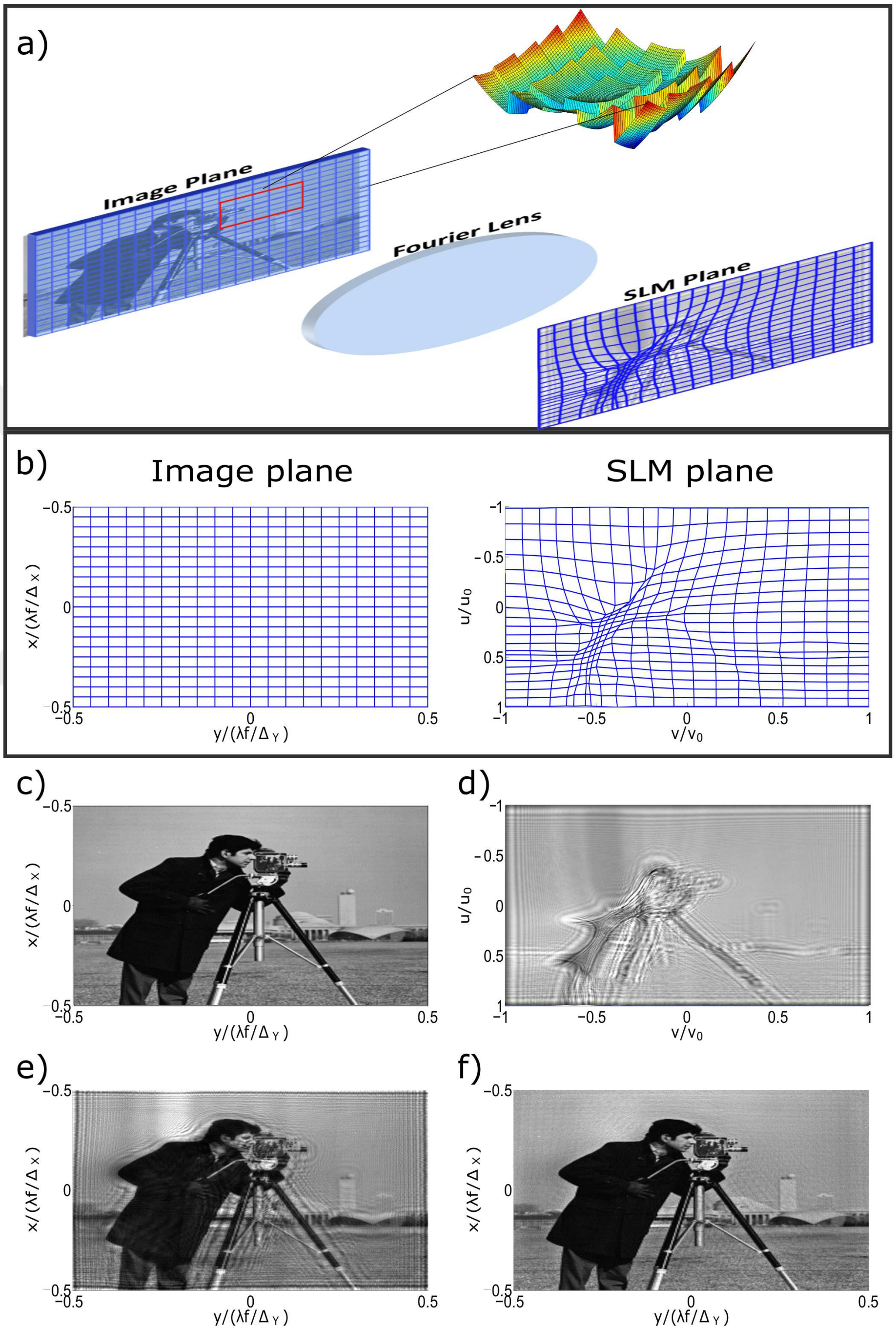

Figure 3.4. Illustration of the proposed method in the 2D signal domain. a) The target image is divided into rectangular blocks. An off-axis lens is imposed on each block. The lenses map the image plane to the SLM plane with a geometrical distortion that uniformizes the energy distribution. b) The rectangular image blocks are mapped into non-overlapping quadrilaterals. The area of each quadrilateral is proportional to the energy content of the associated image block. c) Target image, *Cameraman*. d) The magnitude of the CGH obtained by the designed image specific phase term. e) Reconstruction obtained with direct quantization. f) Reconstruction after 20 IFTA iterations.

the designed phase term $\phi(x, y)$ when the number of blocks are taken as 120×120. Fig. 3.5(b) shows the magnitude of resulting CGH obtained by imposing the phase term in Fig. 3.5(a) on the square root of *Lena* and taking an IFT. Fig. 3.5(c) shows the reconstruction when the CGH in Fig. 3.5(b) is directly quantized into a phase-CGH by discarding the magnitude information. Although intensity is generally replicated and speckle noise is almost absent, the image suffers from some diffraction artifacts and sort of a defocus effect, which is mainly because of the fact that $\phi(x, y)$ performs the mapping in Eq. 3.10 (hence the energy uniformization) only approximately. Nonetheless, the provided metrics (see Table 1) indicate that the reconstruction has a low error value, suggesting that nice results can be obtained when the CGH in Fig. 3.5(b) is used as the initial point for iterative algorithms. In this line, we applied IFTA iterations on Fig. 3.5(b) and obtained the reconstructions in Figs. 3.5(d-f) where we used 2, 5 and 20 iterations, respectively. Fig. 3.5(d) indicates that the defocus effect in Fig. 3.5(c) can be reduced by only 2 iterations, which may constitute the minimum acceptable quality. Fig. 3.5(e) shows that around 10 iterations are needed to suppress diffraction artifacts, and Fig. 3.5(f) shows that in around 20 iterations, it is possible to achieve an unprecedentedly high image quality in coherent image reconstruction.

Table 2 reports the average value of quality metrics when the proposed method is applied in combination with IFTA on a set of 8 gray level images including *Lena, Cameraman, Boat, Mandrill, Peppers, Lake, Pirate, Livingroom* [65]. Note that on this table, rather than the average SC value, we report the average percentage change in SC, Δ_{SC} as defined in Eq. (3.14), since the SC metric has a non-zero value even for an ideal image and absolute SC values are different for different images.

$$SC_I = \sigma_I / \bar{I} \ \ , \ \ SC_{I_R} = \sigma_{I_R} / \bar{I}_R \ \ , \ \ \Delta_{SC} = 100 \times \frac{|SC_I - SC_{I_R}|}{SC_I} \tag{3.14}$$

In Eq. (3.14), I and I_R denote target and reconstructed intensities, respectively. While σ is representing the associated standard deviations, $\bar{I}$ and $\bar{I}_R$ are the mean intensity values.

In order to provide a comparison with the alternative schemes depicted in

Fig.1 3.1(b) and Fig. 3.1(c), we conducted the simulations in Fig. 3.6. All three images are obtained by performing 10 IFTA iterations, but they start with different initial phase terms applied on the target image. The initial term is random, QPF, and our term in Fig. 3.6(a-c), respectively. Fig. 3.6(a) generally reconstructs the gray level variation, but suffers significantly from speckle noise ($SC = 76.17\%$), which stays persistent despite the 10 iterations, leading to poor image quality (pSNR ≈ 30.5dB and SSIM≈ 37). Fig. 3.6(b), thanks to the non-random nature of QPF term, has significantly reduced speckle noise with an SC that shows less than one percent deviation from that of original image. However, the gray level reconstruction is relatively poor (pSNR ≈ 30.78 and SSIM ≈ 56.3), which is mainly due to the fact that the energy is not uniformly distributed on the image plane in the beginning, resulting again in convergence to some local optimum. Finally, Fig. 3.6(b) indicates that the proposed method manages to simultaneously suppress speckle and reproduce gray level (pSNR ≈ 43.86 and SSIM $\approx 71, 2$).

In Table 3, we report the average values of quality metrics when the three methods discussed above are applied on the set of images used in Table 2. For the same set of images, Fig. 3.7 shows the average MSE versus number of iteration curves for the three methods. As seen, when a random phase term is used, the starting MSE value is the highest. With a QPF term, that value is somewhat lowered, but the curves indicate that both methods lead almost to the same final MSE value, and the convergence is rather slow. On the other hand, when our phase term is used, the iterations already start from a very low MSE value (much lower than the values finally converged by the other two cases). Thus, with only a few iterations, very low MSE values are attained, suggesting that whereas other methods are trapped at local optimums, our solution manages to reach almost global optimum. We ascribe this outcome to the fact that in our method, iterations are responsible mainly for fine tuning (we already start from a CGH that is coarse tuned), while in the other methods, iterations should perform both fine and coarse tuning.

In closing this section, we note that apart from the computational complexity of IFTA, our method involves the cost of pre-processing the image blocks to determine the proposed phase function consisting of off-axis aberrated lenses. Though the operations performed per block have an insignificant cost, the total cost for all blocks may be significant, especially in real-time applications. Therefore, it is desired to use as few

Table 3.1. Quality metrics of reconstructions shown in Fig. 3.5.

Number of Iterations	pSNR (dB)	Speckle Contrast (Δ_{SC}) (%)	Structural Similarity Index (SSIM) (max: 100)
0	40	14.25	51.52
2	41.81	6.55	67.4
5	43	5.4	71.2
20	44.65	4.2	82.64

Table 3.2. Quality metrics of reconstructions attained by the proposed method followed by different number of iterations. The values are averaged over a set of 8 target images.

Number of Iterations	pSNR (dB) (average)	Speckle Contrast (Δ_{SC}) (%) (average)	Structural Similarity Index (SSIM) (max: 100) (average)
0	37.21	10.62	50.88
2	39.03	7.58	63.78
5	40.41	6.01	71.38
10	41.6	4.72	76.58
20	42.86	3.52	82.38

blocks as possible. However, as we noted in Section 3, the energy uniformization performed by the block based phase term is only approximate, worsening as the block size grows. To make an assessment, we applied our algorithm using different block sizes on the set of images used in Tables 2 and 3 and plotted the average iteration curves, as shown in Fig. 3.8. The figure indicates that when the number of iterations is sufficiently large, all curves almost converge to the same final MSE value. However, when number of blocks are small, starting MSE values are higher and convergences are slower, hence more iterations are needed for better results. Our trials indicate that using 60×60 blocks provide a good balance between the pre-processing cost and the cost of required iterations.

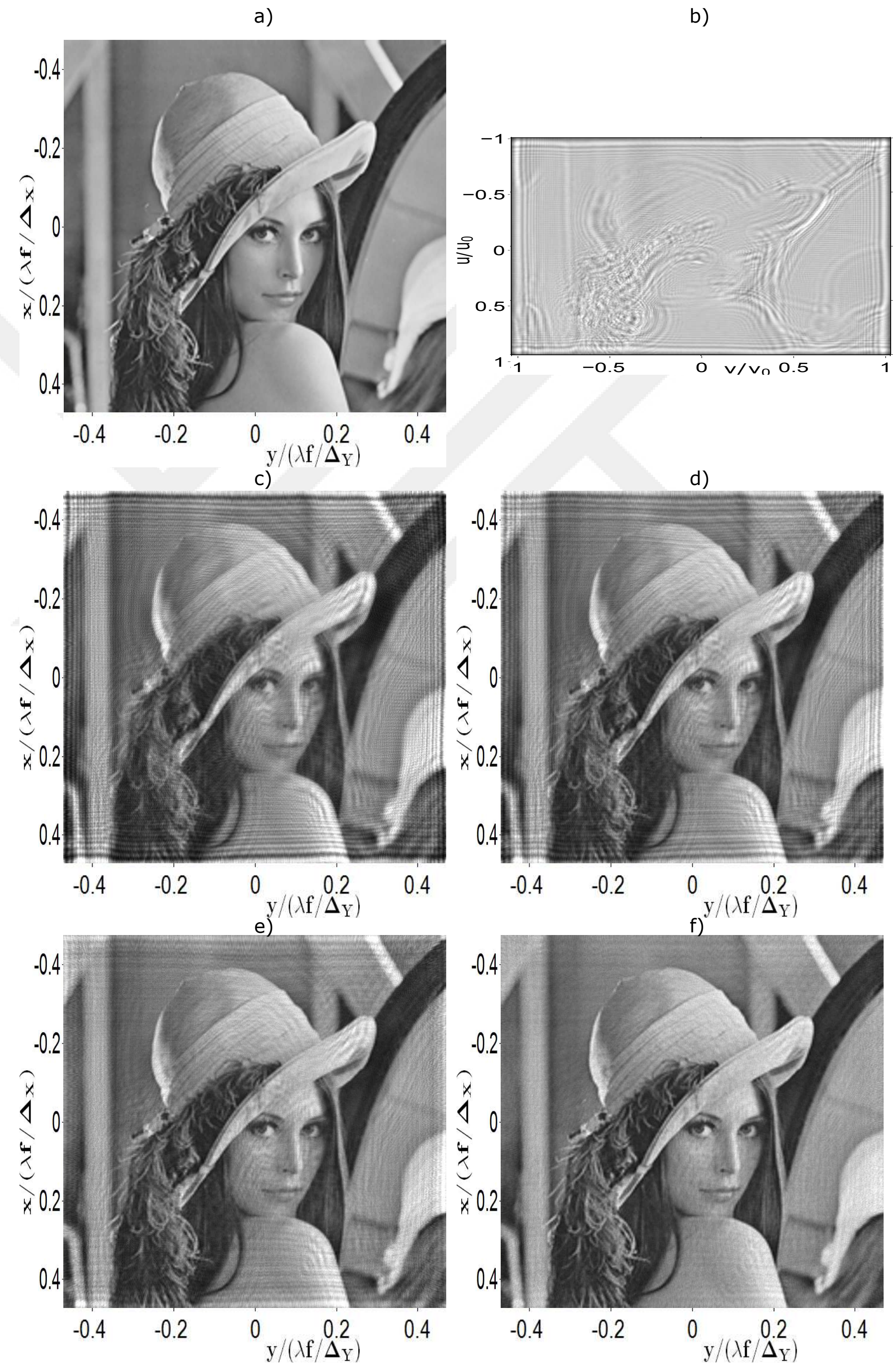

Figure 3.5. a) Target intensity/Computed phase function $\phi(x, y)$. b) Magnitude of the CGH on SLM. c-f) Intensity reconstructions attained by 0, 2, 5 and 20 IFTA iterations, respectively.

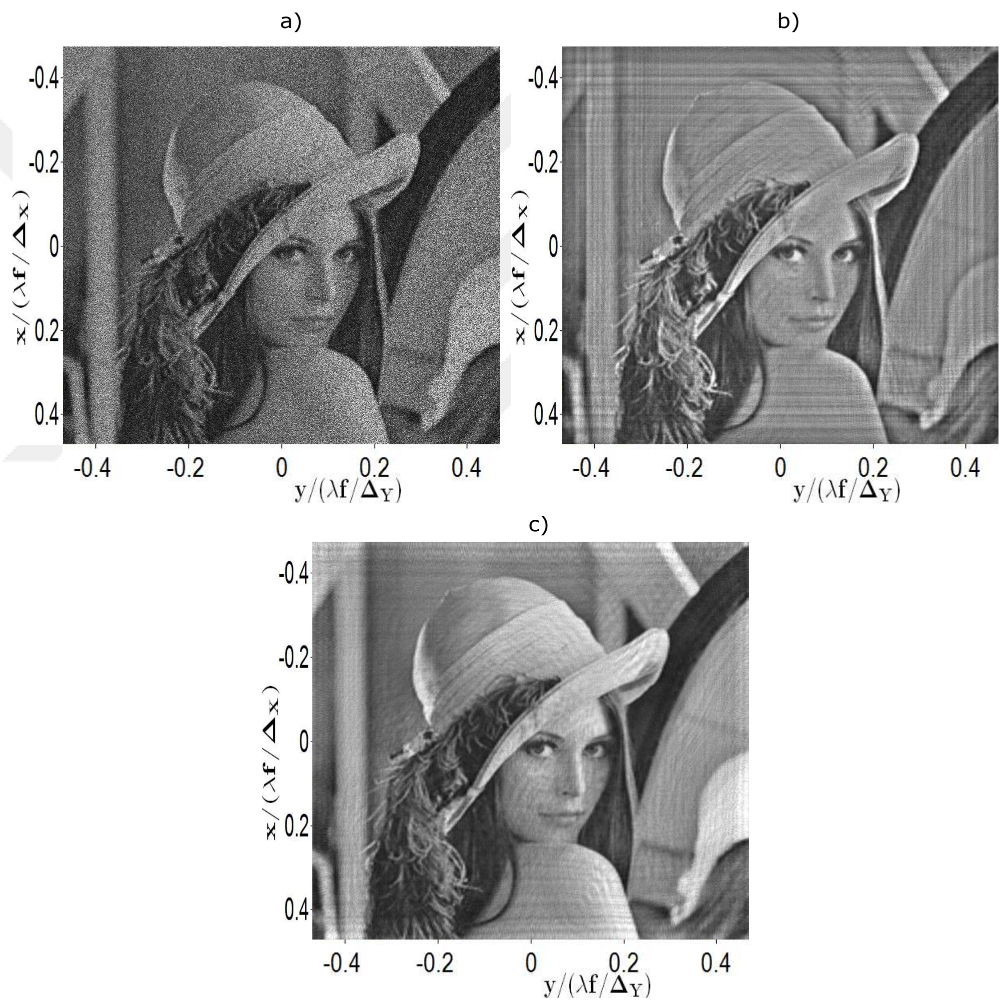

Figure 3.6. Intensity reconstructions of CGHs computed by 10 IFTA iterations when the initial CGH is obtained by imposing a) random phase, b) QPF, c) proposed phase term on the target image.

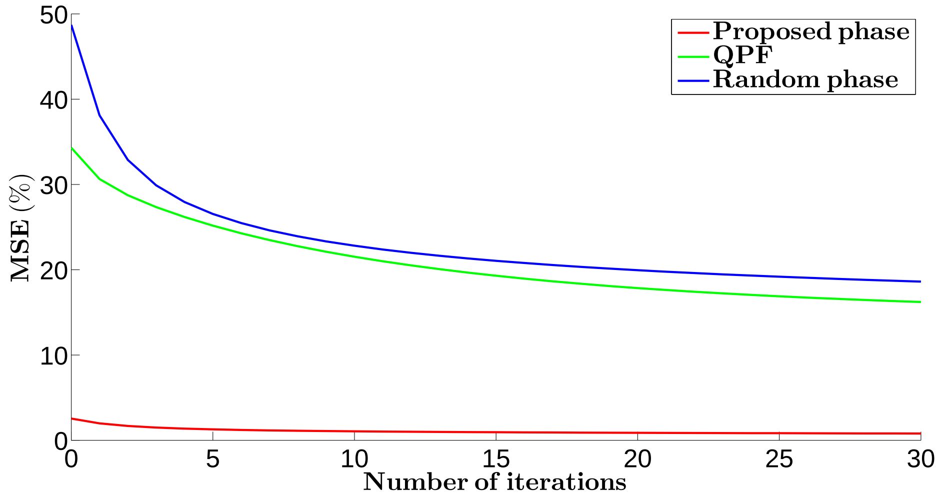

Figure 3.7. Mean square error (MSE) convergence curves of iterated CGHs when random (blue), QPF (green) and proposed (red) phase terms are applied on the target image.

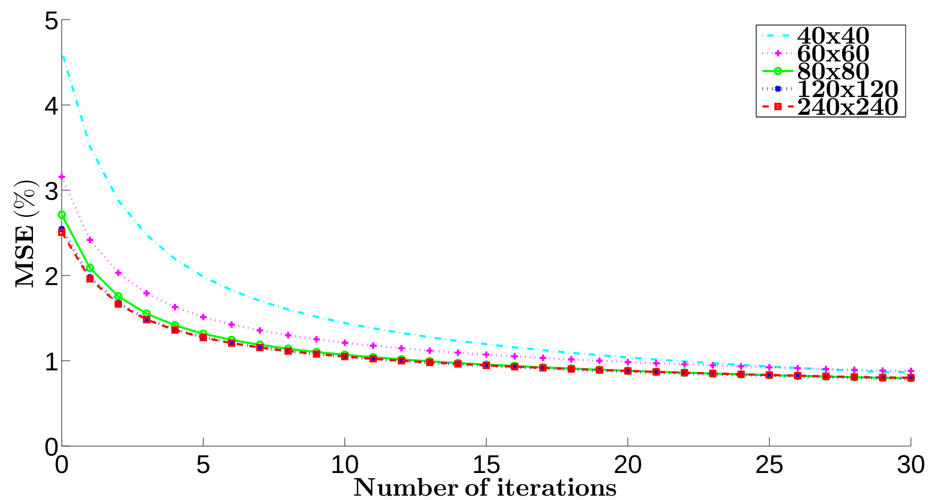

Figure 3.8. MSE convergence curves of iterated CGHs computed by the proposed phase terms for differently sized image blocks. $120x120$ array of blocks are used in the simulations shown in Figs. 3.5 and 3.6.

Table 3.3. Quality metrics of reconstructions attained by 10 iterations for different initial phase terms. The values are averaged over a set of 8 target images.

Phase Type	pSNR (dB) (average)	Speckle Contrast (Δ_{SC}) (%) (average)	Structural Similarity Index (SSIM) (average)
Random Phase	30.48	68.78	36
QPF	30.7	5.34	56.66
Proposed Phase	41.6	4.70	76.58

3.5 Experimental results

We performed experiments with a Holoeye-Pluto phase-only SLM having $8\mu m$ pixel pitch and 8-bit modulation depth to verify our method. In particular, we captured the experimental counterpart of Fig.3.6. The results are presented in Fig.3.9. The results clearly indicate the speckle-free nature of our method relative to the random phase method. Despite the non-idealities in SLM operation such as pixel cross-talk, flickering of liquid crystal cells and contamination with the conjugate and DC beams, the gray level reconstruction capability of our method is also quite evident compared to the QPF based computation.

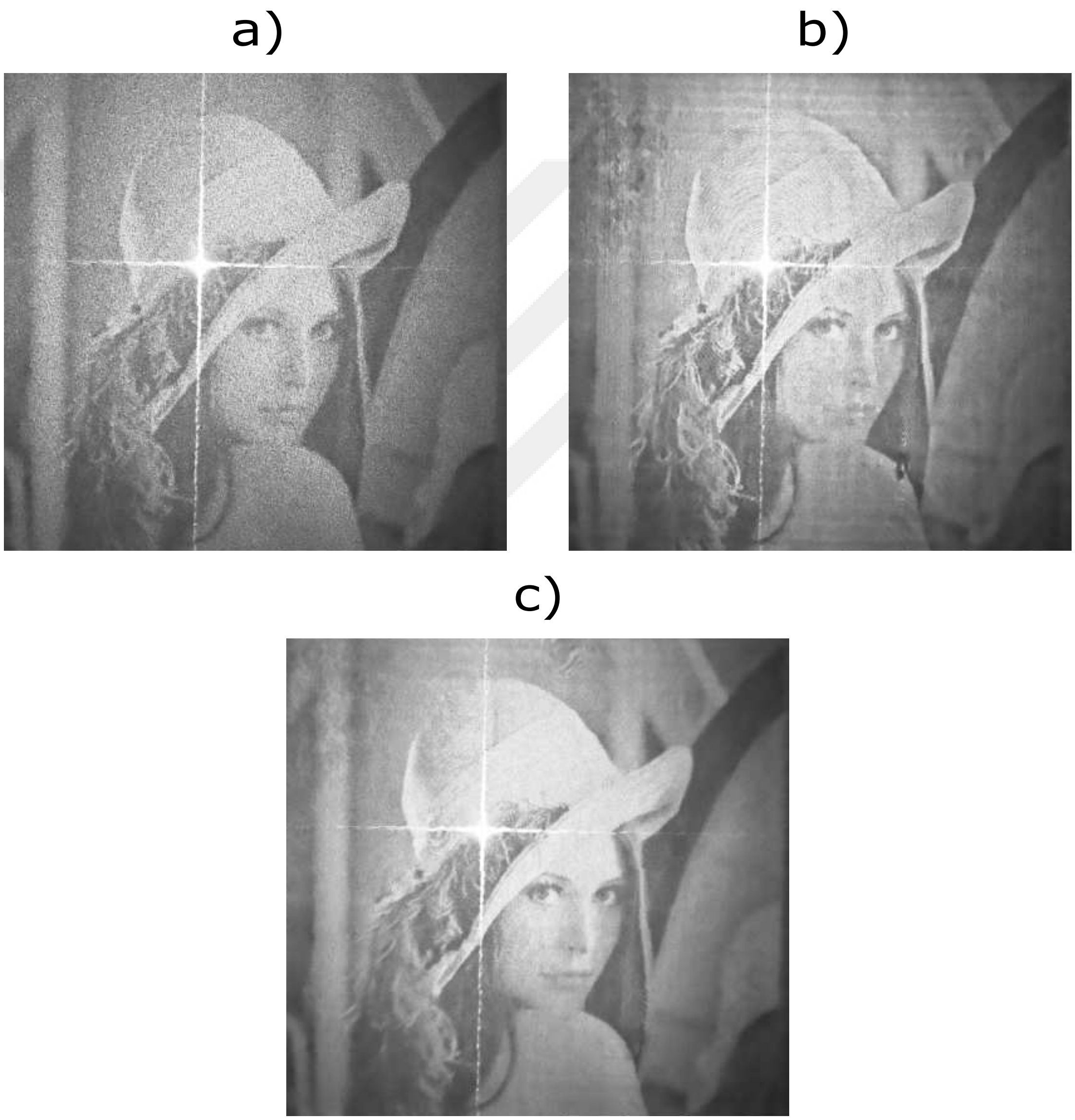

Figure 3.9. Experimental counterpart of Fig. 3.6. a) Random b) QPF c) proposed phase terms. The bright spot appearing on all images is due to the unmodulated beam of the SLM.

4 CONCLUSIONS AND FUTURE WORK

In the first part of this thesis, a fast, non-iterative algorithm to compute phase CGHs is presented for HIP. The greatest advantage of the solution is its quite low computational complexity that well complies with real-time applications. In the examined cases in Section 2.2, Case A requires only a single FFT operation per color channel of a video frame if at most two reconstructions are temporally averaged. If four reconstructions are averaged, two FFTs are needed. In Case B, high image quality readily requires at most two reconstructions to be averaged, so only a single FFT needs to be performed per color channel of a video frame. Another merit of our algorithm is the low speckle noise achieved by the non-random, structured initial phase terms applied on the images.

When current-state of the art phase-only SLM technology and the available frame rates of 60 Hz are considered, it seems that Case B of Section 2.2 has the highest practical applicability potential. 60 fps interlaced video format (in which only half of the spatial resolution is available for each video frame) can be readily delivered with our solution for case B without any frame rate division (of course, color video requires 3 SLMs). The other cases we explored require SLMs with higher frame rates and are more likely to be useful in the future. High quality 60 fps progressive video requires 2 and 4 reconstructions per color channel to be averaged respectively for case B and A, implying SLM frame rates of 120 and 240 Hz per color. Such high frame rates are not possible with the current LCoS phase-SLM technology, but may be attained with newly emerging blue-phase materials [66, 67]. Standard cinema quality low-persistence video operating at 24 fps though requires SLM frame rates of 48 or 96 Hz for each color, which is more likely to be attained.

Despite its high frame rate requirements, Case A is advantageous in that it operates with maximum light efficiency. For this case, under the assumption that the light source already generates polarized light, our simulations indicate a light efficiency of approximately 60%, where light is lost only to the unmodulated beam of the SLM and higher diffraction orders. In case B though, a significant part of the energy appears as encoding noise, decreasing the light efficiency to about 6%. However, we remind that such low efficiency values are also the case in alternative algorithms, so our algorithm does not impose a disadvantage here.

In Chapter 3, we present a novel method for calculating phase CGHs to be used in HIP. Though the algorithms are developed by assuming a FT relation between image and SLM planes, the extension to paraxial systems described by Fresnel or fractional Fourier transforms are straightforward. The algorithm can be extended to non-paraxial systems as well provided that the ray angles emerging from image plane vertices and hitting SLM plane vertices are found, and off-axis lenses designed on each block are updated accordingly.

The simulation results presented in Section 3.4 indicate that the method almost determines the global optimum solution of the phase CGH computation problem in HIP context, without resorting to any compromise in projected image size or light efficiency. To our knowledge, the image presented in Fig.3.5(f) is the lowest error and highest quality image ever reconstructed and presented by a phase CGH, with an MSE value about 20X smaller than what is achievable by existing methods for full FOV. The overall computational complexity is similar to that of existing alternatives.

In our view, the method owes its success to the fact that full physical as well as mathematical insight is incorporated during its development. While almost all existing methods merely formulate the phase CGH computation problem as a purely mathematical optimization problem, the presented method uses the very important physical insights depicted in Fig. 3.1 and the physical interpretations of phase functions and instantaneous frequencies in terms of ray angles, lenses, prisms, etc. In our belief, the method also constitutes a nice example of the application of the powerful concept of space-frequency (phase-space) analysis in the CGH domain.

In a nutshell, two novel phase CGH algorithm are devised, implemented, analysed and compared with the existing methods regarding both final image quality, light efficiency, attainable FOV and computational cost. All of these parameters have been tried to be optimized by exploiting mathematical concepts, tools, functions as well as optical observations, insights, analysis and design procedures. Thereby, the obtained results are closer to global optimums than any other previous methods. Hence, we believe that this thesis provides substantial insight and information towards comprehending the fundamental limits of the phase-only holography.

Bibliography

[1] D. Gabor *et al.*, “A new microscopic principle,” *Nature*, vol. 161, no. 4098, pp. 777–778, 1948.

[2] A. Greenbaum, W. Luo, T.-W. Su, Z. Göröcs, L. Xue, S. O. Isikman, A. F. Coskun, O. Mudanyali, and A. Ozcan, “Imaging without lenses: achievements and remaining challenges of wide-field on-chip microscopy,” *Nature methods*, vol. 9, no. 9, pp. 889–895, 2012.

[3] D. Psaltis, D. Brady, X.-G. Gu, and S. Lin, “Holography in artificial neural networks,” *Nature*, vol. 343, no. 6256, pp. 325–330, 1990.

[4] G. K. Ackermann and J. Eichler, *Holography: a practical approach*. John Wiley & Sons, 2007.

[5] O. K. Ersoy, *Diffraction, fourier optics and imaging*, vol. 30. John Wiley & Sons, 2006.

[6] A. W. Lohmann and D. Paris, “Binary fraunhofer holograms, generated by computer,” *Applied Optics*, vol. 6, no. 10, pp. 1739–1748, 1967.

[7] L. Lesem, P. Hirsch, and J. Jordan, “The kinoform: a new wavefront reconstruction device,” *IBM Journal of Research and Development*, vol. 13, no. 2, pp. 150–155, 1969.

[8] B. Brown and A. Lohmann, “Computer-generated binary holograms,” *IBM Journal of research and Development*, vol. 13, no. 2, pp. 160–168, 1969.

[9] M. Reicherter, T. Haist, E. Wagemann, and H. Tiziani, “Optical particle trapping with computer-generated holograms written on a liquid-crystal display,” *Optics letters*, vol. 24, no. 9, pp. 608–610, 1999.

[10] T. Nobukawa, Y. Wani, and T. Nomura, “Multiplexed recording with uncorrelated computer-generated reference patterns in coaxial holographic data storage,” *Optics letters*, vol. 40, no. 10, pp. 2161–2164, 2015.

[11] I. Dolev, I. Epstein, and A. Arie, "Surface-plasmon holographic beam shaping," *Physical review letters*, vol. 109, no. 20, p. 203903, 2012.

[12] K.-Y. Hsu, H.-Y. Li, and D. Psaltis, "Holographic implementation of a fully connected neural network," *Proceedings of the IEEE*, vol. 78, no. 10, pp. 1637–1645, 1990.

[13] M. Neil, M. Booth, and T. Wilson, "Dynamic wave-front generation for the characterization and testing of optical systems," *Optics letters*, vol. 23, no. 23, pp. 1849–1851, 1998.

[14] B. Javidi and F. Okano, *Three-dimensional television, video, and display technologies*. Springer Science & Business Media, 2002.

[15] M. Makowski, M. Sypek, I. Ducin, A. Fajst, A. Siemion, J. Suszek, and A. Kolodziejczyk, "Experimental evaluation of a full-color compact lensless holographic display," *Optics express*, vol. 17, no. 23, pp. 20840–20846, 2009.

[16] A. Georgiou, J. Christmas, N. Collings, J. Moore, and W. Crossland, "Aspects of hologram calculation for video frames," *Journal of Optics A: Pure and Applied Optics*, vol. 10, no. 3, p. 035302, 2008.

[17] E. Buckley, "Holographic laser projection," *Journal of display technology*, vol. 7, no. 3, pp. 135–140, 2011.

[18] E. Buckley, "Holographic projector using one lens," *Optics letters*, vol. 35, no. 20, pp. 3399–3401, 2010.

[19] A. Georgiou, J. Christmas, J. Moore, A. Jeziorska-Chapman, A. Davey, N. Collings, and W. Crossland, "Liquid crystal over silicon device characteristics for holographic projection of high-definition television images," *Applied optics*, vol. 47, no. 26, pp. 4793–4803, 2008.

[20] U. Efron, *Spatial light modulator technology: materials, devices, and applications*, vol. 47. CRC Press, 1994.

[21] G. Lazarev, A. Hermerschmidt, S. Krüger, and S. Osten, "Lcos spatial light modulators: trends and applications," 2012.

[22] R. Tudela, I. Labastida, S. Vallmitjana, I. Juvells, A. Carnicer, *et al.*, "Full complex fresnel holograms displayed on liquid crystal devices," *Journal of Optics A: Pure and Applied Optics*, vol. 5, no. 5, p. S189, 2003.

[23] A. Shibukawa, A. Okamoto, Y. Goto, S. Honma, and A. Tomita, "Digital phase conjugate mirror by parallel arrangement of two phase-only spatial light modulators," *Optics express*, vol. 22, no. 10, pp. 11918–11929, 2014.

[24] E. Ulusoy, L. Onural, and H. M. Ozaktas, "Full-complex amplitude modulation with binary spatial light modulators," *JOSA A*, vol. 28, no. 11, pp. 2310–2321, 2011.

[25] V. Arrizón, G. Méndez, and D. Sánchez-de La-Llave, "Accurate encoding of arbitrary complex fields with amplitude-only liquid crystal spatial light modulators," *Optics express*, vol. 13, no. 20, pp. 7913–7927, 2005.

[26] F. Mok, J. Diep, H.-K. Liu, and D. Psaltis, "Real-time computer-generated hologram by means of liquid-crystal television spatial light modulator," *Optics Letters*, vol. 11, no. 11, pp. 748–750, 1986.

[27] M. A. Seldowitz, J. P. Allebach, and D. W. Sweeney, "Synthesis of digital holograms by direct binary search," *Applied Optics*, vol. 26, no. 14, pp. 2788–2798, 1987.

[28] E. Ulusoy, L. Onural, and H. M. Ozaktas, "Synthesis of three-dimensional light fields with binary spatial light modulators," *JOSA A*, vol. 28, no. 6, pp. 1211–1223, 2011.

[29] K. V. Chellappan, E. Erden, and H. Urey, "Laser-based displays: a review," *Applied optics*, vol. 49, no. 25, pp. F79–F98, 2010.

[30] S. Weissbach and F. Wyrowski, "Error diffusion procedure: theory and applications in optical signal processing," *Applied optics*, vol. 31, no. 14, pp. 2518–2534, 1992.

[31] F. Wyrowski, "Diffractive optical elements: iterative calculation of quantized, blazed phase structures," *JOSA A*, vol. 7, no. 6, pp. 961–969, 1990.

[32] J. R. Fienup, "Reconstruction of an object from the modulus of its fourier transform," *Optics letters*, vol. 3, no. 1, pp. 27–29, 1978.

[33] J. R. Fienup, “Phase retrieval algorithms: a comparison,” *Applied optics*, vol. 21, no. 15, pp. 2758–2769, 1982.

[34] J. Fienup, “Iterative method applied to image reconstruction and to computer-generated holograms,” *Optical Engineering*, vol. 19, no. 3, pp. 193297–193297, 1980.

[35] R. Liu, B.-Y. Gu, B.-Z. Dong, and G.-Z. Yang, “Design of diffractive phase elements that realize axial-intensity modulation based on the conjugate-gradient method,” *JOSA A*, vol. 15, no. 3, pp. 689–694, 1998.

[36] F. Wyrowski and O. Bryngdahl, “Speckle-free reconstruction in digital holography,” *JOSA A*, vol. 6, no. 8, pp. 1171–1174, 1989.

[37] E. Ulusoy, *Signal processing based solutions for holographic displays that use binary spatial light modulators*. PhD thesis, Bilkent University, 2012.

[38] F. Wyrowski and O. Bryngdahl, “Iterative fourier-transform algorithm applied to computer holography,” *JOSA A*, vol. 5, no. 7, pp. 1058–1065, 1988.

[39] R. W. Gerchberg and W. O. Saxton, “A practical algorithm for the determination of the phase from image and diffraction plane pictures,” *Optik (Jena)*, vol. 35, pp. 237+, 1972.

[40] S. P. Poland, N. Krstajić, R. D. Knight, R. K. Henderson, and S. M. Ameer-Beg, “Development of a doubly weighted gerchberg–saxton algorithm for use in multibeam imaging applications,” *Optics letters*, vol. 39, no. 8, pp. 2431–2434, 2014.

[41] R. G. Dorsch, A. W. Lohmann, and S. Sinzinger, “Fresnel ping-pong algorithm for two-plane computer-generated hologram display,” *Applied optics*, vol. 33, no. 5, pp. 869–875, 1994.

[42] H. Akahori, “Spectrum leveling by an iterative algorithm with a dummy area for synthesizing the kinoform,” *Applied optics*, vol. 25, no. 5, pp. 802–811, 1986.

[43] R. Eschbach and Z. Fan, “Complex-valued error diffusion for off-axis computer-generated holograms,” *Applied optics*, vol. 32, no. 17, pp. 3130–3136, 1993.

[44] E. Barnard, "Optimal error diffusion for computer-generated holograms," *JOSA A*, vol. 5, no. 11, pp. 1803–1817, 1988.

[45] R. Floyd and L. Steinberg, "An adaptive algorithm for spatial grayscale," *Proceedings of the society for information display*, no. 17, pp. 78–84, 1976.

[46] M. El Bouz and K. Heggarty, "Signal window minimum average error algorithm for multi-phase level computer-generated holograms," *Optics Communications*, vol. 180, no. 1, pp. 21–28, 2000.

[47] R. Eschbach, "Comparison of error diffusion methods for computer-generated holograms," *Applied optics*, vol. 30, no. 26, pp. 3702–3710, 1991.

[48] F. Fetthauer, S. Weissbach, and O. Bryngdahl, "Equivalence of error diffusion and minimal average error algorithms," *Optics communications*, vol. 113, no. 4, pp. 365–370, 1995.

[49] N. Yoshikawa and T. Yatagai, "Phase optimization of a kinoform by simulated annealing," *Applied optics*, vol. 33, no. 5, pp. 863–868, 1994.

[50] J. Zhuang and O. Ersoy, "Fast decimation-in-frequency direct binary search algorithms for synthesis of computer-generated holograms," *JOSA A*, vol. 11, no. 1, pp. 135–143, 1994.

[51] R. Liu, B.-Z. Dong, G.-Z. Yang, and B.-Y. Gu, "Generation of pseudo-nondiffracting beams with use of diffractive phase elements designed by the conjugate-gradient method," *JOSA A*, vol. 15, no. 1, pp. 144–151, 1998.

[52] C. Hsueh and A. Sawchuk, "Computer-generated double-phase holograms," *Applied optics*, vol. 17, no. 24, pp. 3874–3883, 1978.

[53] M. Hayes, "The reconstruction of a multidimensional sequence from the phase or magnitude of its fourier transform," *IEEE Transactions on Acoustics, Speech, and Signal Processing*, vol. 30, no. 2, pp. 140–154, 1982.

[54] V. Arrizón and D. Sánchez-de-la Llave, "Double-phase holograms implemented with phase-only spatial light modulators: performance evaluation and improvement," *Applied optics*, vol. 41, no. 17, pp. 3436–3447, 2002.

[55] D. Mengu, E. Ulusoy, and H. Urey, “Holographic image projection with phase only spatial light modulators via non-iterative cgh computation method,” in *Digital Holography and Three-Dimensional Imaging*, pp. DT2A–5, Optical Society of America, 2015.

[56] D. Mengu, E. Ulusoy, and H. Urey, “Non-iterative phase hologram computation for low speckle holographic image projection,” *Optics Express*, vol. 24, no. 5, pp. 4462–4476, 2016.

[57] D. Abookasis and J. Rosen, “Three types of computer-generated hologram synthesized from multiple angular viewpoints of a three-dimensional scene,” *Applied optics*, vol. 45, no. 25, pp. 6533–6538, 2006.

[58] T. Shimobaba and T. Ito, “Random phase-free computer-generated hologram,” *Optics express*, vol. 23, no. 7, pp. 9549–9554, 2015.

[59] Z. Wang, A. C. Bovik, H. R. Sheikh, and E. P. Simoncelli, “Image quality assessment: from error visibility to structural similarity,” *IEEE transactions on image processing*, vol. 13, no. 4, pp. 600–612, 2004.

[60] J. W. Goodman, *Introduction to Fourier optics*. Roberts and Company Publishers, 2005.

[61] F. Wyrowski, R. Hauck, and O. Bryngdahl, “Computer holography: object dependent deterministic diffusers,” *Optics communications*, vol. 63, no. 2, pp. 81–84, 1987.

[62] W. Dallas, “Deterministic diffusers for holography,” *Applied optics*, vol. 12, no. 6, pp. 1179–1187, 1973.

[63] A. Papoulis, “Random variables, and stochastic processes,” 1990.

[64] J. W. Goodman, “Some fundamental properties of speckle,” *JOSA*, vol. 66, no. 11, pp. 1145–1150, 1976.

[65] S. L. E. Rafael C. Gonzalez, Richard E. Woods, “ImageProcessingPlace.com.” http://www.imageprocessingplace.com/, 2008. [Online; accessed 28-July-2015].

[66] J. Yan, Y. Xing, Z. Guo, and Q. Li, “Low voltage and high resolution phase modulator based on blue phase liquid crystals with external compact optical system,” *Optics express*, vol. 23, no. 12, pp. 15256–15264, 2015.

[67] Y.-H. Lin, H.-S. Chen, H.-C. Lin, Y.-S. Tsou, H.-K. Hsu, and W.-Y. Li, "Polarizer-free and fast response microlens arrays using polymer-stabilized blue phase liquid crystals," *Applied Physics Letters*, vol. 96, no. 11, p. 113505, 2010.